

# Bibliography

## A

**ASME standards (2006)**, “ASME V&V 10-2006 Guide for Verification and Validation in Computational Solid Mechanics”, The American Society of Mechanical Engineers, New York

**ASTM Standard E 140-02 (2002)**, “Standard Hardness Conversion Tables for Metals. Relationship Among Brinell Hardness, Vickers Hardness, Rockwell Hardness, Superficial Hardness, Knoop Hardness, and Scleroscope Hardness”, *ASTM International*, West Conshohocken, PA, USA

## B

**Babuska, I. and Oden, J.T. (2004)**, “Verification and validation in computational engineering and science: basic concepts.”, *Comput. Methods Appl. Mech. Engrg.* 193:4057-4066

**Bernard, J.E. and Clover, C.L. (1994)**, “Validation of Computer Simulations of Vehicle Dynamics”. *SAE Transactions*, 940231

## C

**Callister, W.D. (2003)**, “Material Science and Engineering - An Introduction”, 6th ed., Wiley, Hoboken, NJ

**Cebon, D. (1986)**, “Simulation of the Response of Leaf Springs to Broad Band Random Excitation”, *Vehicle System Dynamics*, Vol. 15, No.6, pp. 375-392

**Cole, D.J. and Cebon, D. (1994)**, “Predicting Vertical Dynamic Tire Forces of Heavy Trucks”, *Vehicle-Road Interaction, ASTM STP 1225*, B. T. Kulakowski, Ed., American Society for Testing and Materials, Philadelphia, pp. 27-35

**Cosme, C., Ghasemi, A. and Gandevia, J. (1999)**, “Application of Computer Aided Engineering in the Design of Heavy-Duty Truck Frames”, *SAE Transactions*, 1999-01-3760

**Czichos, H. (1978)**, “Tribology – A systems approach to the science and technology of friction, lubrication and wear”, Elsevier, New York

## D

**Dowling, N.E. (1999)**, “Mechanical behavior of materials – Engineering methods for deformation, fracture and fatigue”, 2nd ed., Prentice Hall, Upper Saddle River, NJ

**Dreyfus, G. (2005)**, “Neural networks – Methodology and applications”, Springer-verlag, Heidelberg, New York

## E

**Edara, R. Shih, S., Tamini, N., Palmer, T. and Tang, A. (2005)**, “Heavy Vehicle Suspension Frame Durability Analysis Using Virtual Proving Ground”, *SAE Transactions*, 2005-01-3609

**ELMadany, M.M. (1987)**, “Nonlinear ride analysis of heavy trucks”, *Computers & Structures*, Vol. 25, No. 1, pp. 69-82

**Ekici, B. (2005)**, “Multi-response optimisation in a three-link leaf-spring model”, *Int. J. Vehicle Design*, Vol. 38, No.4, pp. 326-346

## F

**Fancher, P.S., Ervin, R.D., MacAdam, C.C, and Winkler, C.B. (1980)**, “Measurement and Representation of the Mechanical Properties of Truck Leaf Springs”, SAE Technical Paper 800905

**Ferry, W.B., Frise, P.R., Andrews, G.T. and Malik, M.A. (2002)**, “Combining virtual simulation and physical vehicle test data to optimize durability testing”, *Fatigue & Fracture of Engineering Materials and Structures*, Vol. 25, Issue 12, pp.1127-1134

**Figliola, R.S. and Beasley, D.E. (2006)**, “Theory and Design for Mechanical Measurements”, Fourth Edition, Wiley and Sons.

## G

**Geers, T.L. (1984)**, “An objective error measure for the comparison of calculated and measured transient response histories”, *The shock and vibration bulletin*, 54:99-107

**Gere, J.M. (2004)**, “Mechanics of materials”, 6th ed., Brooks/Cole, Belmont, California

**Ghazi Zadeh, A., Fahim, A. and El-Gindy, M. (2000)**, “Neuro-leaf spring”, *Heavy Vehicle Systems, A Series of the International Journal of Vehicle Design*, Vol. 7, No. 4, pp. 317-335

## H

**Hagan, M.T., Howard, B.D. and Beale, M. (1996)**, “Neural network design”, PWS publishing company, Boston, MA

**Heydinger G.J., Garrot W.R., Chrstos J.P. and Guenther D.A. (1990)**, “A Methodology for Validating Vehicle Dynamics Simulations”, *SAE Technical Paper 900128*

**Hoyle, J.B. (2004)**, “Modelling the static stiffness and dynamic frequency response characteristics of a leaf spring truck suspension”, *Proc. of IMechE, Part D: J. Automobile Engineering*, Vol. 218, pp. 259-278

**Huhtala, M., Vesimaki, M. and Halonen, P. (1994)**, “Computer Simulation of Road-Vehicle Dynamic Interaction Forces of Three-and Four-Axle Trucks”, in Kulakowski, B.T. (Ed.): *Vehicle –Road Interaction*, pp.36-51, ASTM STP 1225, American Society for Testing and Materials, Philadelphia

## J

**Jayakumar, P., Alanoly, J. and Johnson, R. (2005)**, “Three-Link Leaf-Spring Model for Road Loads”, *SAE Technical Paper 2005-01-0625*

## K

**Kat, C. and Els, P.S. (2011)**, “Importance of correct validation of simulation models”, *Proc. ASME 2011 International Design Engineering Technical Conferences & Computers and Information in Engineering Conferences*, Aug. 29-31, Washington, DC, USA

**Kyowa (2011)**, Available at <http://www.kyowa-ei.co.jp/english/products/gages/pdf/bridge.pdf>, [Accessed on 09 July 2011]

## L

**Li, Q. and Li, W. (2004)**, “A Contact finite element algorithm for the multileaf spring of vehicle suspension systems”, *IMEC-E Part D: J. Autom. Engrg.*, Vol. 218, pp. 305-314

## M

- Merkle, A.P and Marks, L.D. (2007)**, “A predictive analytical friction model from basic theories of interfaces, contacts and dislocations”. *Tribology Letters*, Vol. 26, No.1, pp. 73-84
- Milliken, W.F. and Milliken, D.L. (2002)**, “Chassis Design: Principles and Analysis”, SAE, Warrendale, PA.
- Monroe (2011)** Monroe Shocks and Struts, [Online] available at <http://www.monroe.com.au/trade-corner/tech-info/suspension-systems/rear-suspensions.html> (Accessed on 11 Oktober 2011)
- Moon, I.d., Kim, G.t., Lim, J.h. and Hwang, Y. (2007)**, “A Flexible Multi-Body Dynamic Model for Analyzing the Hysteretic Characteristics and the Dynamic Stress of a Taper Leaf Spring”, *SAE Technical Paper 2007-01-0852*
- Müller, B., Reinhardt, J. and Strickland, M.T. (1995)**, “Neural networks – An Introduction“, 2nd ed., Springer-Verlag, Heidelberg, New York.

## O

- Oberkampf, W.L. and Barone, M.F. (2006)**, “Measures of agreement between computation and experiment: Validation metrics”, *Journal of Computational Physics*, 217, pp.5-36
- Oberkampf, W.L. and Trucano, T.G. (2002)**, “Verification and validation in computational fluid dynamics”, *Progress in Aerospace Sciences*, Vol. 38 pp. 209-272
- Omar, M.A., Shabana, A.A., Mikkola, A., Loh, W and Basch, R (2004)**, “Multibody System Modeling of Leaf Springs”, *J. of Vibration and Control*, Vol. 10, No. 11, pp.1601-1638
- Oxford Dictionaries (2011)** Dictionary, [Online] available at <http://www.oxforddictionaries.com/definition/tribology?region=us> (Accessed on 19 September 2011)

## P

- Prasade, U., Medepalli, S., Moore, D. and Rao, R.N. (2006)**, “Beam Element Leaf Spring Suspension Model Development and Assessment Using Road Load Data”, *SAE Technical Paper 2006-01-0994*

## Q

**Qin, P., Dentel, G. and Mesh, M. (2002)**, “Multi-leaf spring and Hotchkiss suspension CAE simulation”, *ABAQUS Users’ Conference*

## R

**Rill, G., Kessing, N., Lange, O. and Meier, J. (2003)**, “Leaf Spring Modelling for Real Time Applications”, *Proceedings of International Association of Vehicle System Dynamics (IAVSD) 18<sup>th</sup> Symposium, Atsugi, Japan*

**Roy, C.J. and Oberkampf, W.L. (2011)**, “A comprehensive framework for verification, validation, and uncertainty quantification in scientific computing”, *Computer methods in applied mechanics and engineering*, 200:2131-2144

**Russell, D.M. (1997a)**, “Error Measures for Comparing Transient Data: Part I: Development of a Comprehensive Error Measure”, *Proceedings of the 68<sup>th</sup> Shock and Vibration Symposium, Hunt Valley, MD*, pp. 175 – 184

**Russell, D.M. (1997b)**, “Error Measures for Comparing Transient Data: Part II: Error Measures Case Study”, *68<sup>th</sup> Shock and Vibration Symposium, Hunt Valley, MD*, pp. 185 – 198

## S

**SAE Spring Design Manual (1996)**, 2nd ed., *Society of Automotive Engineers, Inc.*, 400 Commonwealth drive, Warrendale, PA

**Sarin, H., Kokkolaras, M., Hulbert, G., Papalambros, P., Barbat, S. and Yang, R.-J. (2010)**, “Comparing Time Histories for Validation of Simulation Models: Error Measures and Metrics”, *J. Dynamic Systems, Measurement, and Control*, Vol. 132

**Schwer, L.E. (2007)**, “Validation metrics for response histories: perspectives and case studies”, *Engineering with Computers*, 23:295-309

**Sprague, M.A. and Geers, T.L. (2003)**, “Spectral elements and field separation for an acoustic fluid subject to cavitation”, *J. Computational Physics*, 184:149-162

**Sprague, M.A. and Geers, T.L. (2006)**, “A spectral-element/finite-element analysis of a ship-like structure subjected to an underwater explosion”, *Computer methods in applied mechanics and engineering*, 195:2149-2167

**Sugiyama, H., Shabana, A.A., Omar, M.A. and Loh, W. (2006)**, “Development of nonlinear elastic leaf spring model for multibody vehicle systems”, *Computer methods in applied mechanics and engineering*, Vol. 195, pp. 6925-6941

## T

**Tavakkoli, S., Aslani, F., Rohweder, D.S. and Savanur, S. (1996)**, “Analytical predictions of Leaf spring bushing loads using MSC/NASTRAN and MDI/ADAMS”, MSC conference proceedings, viewed 14 October 2011, < [http://www.mscsoftware.com/support/library/conf/wuc96/11b\\_asla.pdf](http://www.mscsoftware.com/support/library/conf/wuc96/11b_asla.pdf)>.

## V

**Van de Wetering Engineering (2001)**, “Owners Handbook”, Rosslyn, South Africa

## W

**West York Steel, (2009)**, Available at: <http://www.westyorkssteel.com/EN19.html> [Accessed on 14 October 2009]

## Y

**Yang, Y., Ren, W., Chen, L., Jiang, M. and Yang, Y. (2007)**, “Study on ride comfort of tractor with tandem suspension based on multi-body system dynamics”, *Applied mathematical modeling*, doi:10.1016/j.apm.2007.10.011

# Appendix A

## Six component load cell (6clc)

This appendix is concerned with the development of the six component load cell. It discusses the calibration of the uni-axial (tension-compression) load cells, the verification of the concept of the 6clc as well as the verification of the model of the 6clc that was created in ADAMS/Car. The verification is done by using the analytical equations that were derived. The validation of both the analytical and ADAMS/Car model against experimental measurements are presented. Paragraph A.1 discusses the calibration of the individual uni-axial load cells and paragraph A.2 discusses the verification and validation of the physical and virtual six component load cell.

### A.1. Calibration of uni-axial load cells

The uni-axial load cell forms the basis of the 6clc. The 6clc is formed by connecting six uni-axial load cells between two parts in such a way that all six degrees of freedom between the two parts are removed. The uni-axial load cells are orientated such that each uni-axial load cell is only in tension or compression. Figure A.1 shows the two parts with the six uni-axial load cells connecting them. Figure A.2 shows one of the uni-axial load cells.

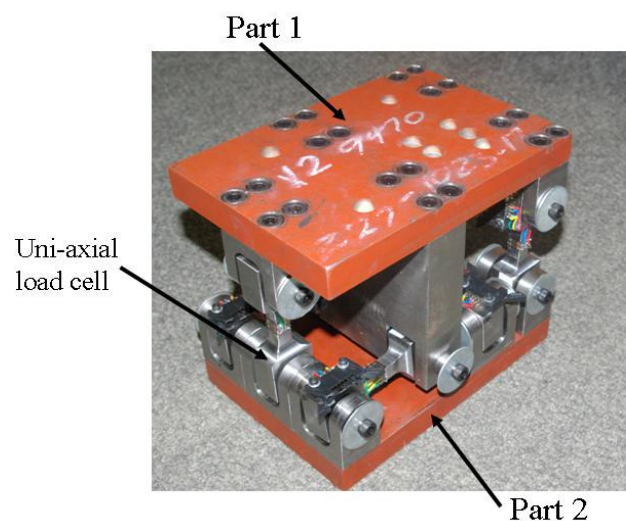


**Figure A.1.** Six component load cell

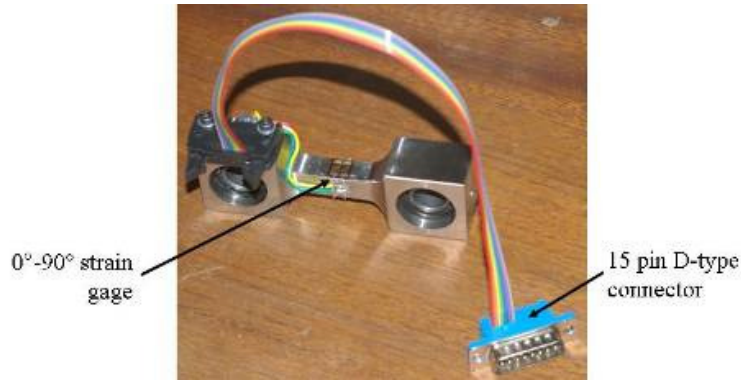


**Figure A.2.** Uni-axial load cell

The uni-axial load cell was designed to be able to handle 5000 kg without yielding and with a cross-sectional area that will give good sensitivity for the strain measurements. In order to measure the strain two 0°-90° strain gages were placed on opposite sides of the reduced cross-sectional area of the uni-axial load cell (see Figure A.2). A full bridge configuration was used as shown in Figure A.3. This configuration allows for temperature compensation, the cancellation of the thermal effect of the lead wires as well as cancelling bending. It is not expected that the uni-axial load cells will have any bending imposed on them as they will be connected to the two parts in the 6clc via spherical bearings.

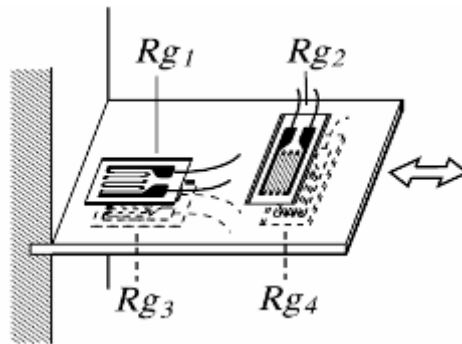


**Figure A.3.** Full bridge configuration used in uni-axial load cells (Kyowa, 2011)

The force is obtained from the uni-axial load cell by taking the measured strain ( $\epsilon$ ) and multiplying it by the Young’s Modulus ( $E$ ) of the material and the cross-sectional area ( $A$ ) of the uni-axial load cell (Eq.{A.1}). The cross-sectional area of each of the uni-axial load cells were measured with a micrometer. The cross-sectional areas of each of the uni-axial load cells are given in Table A.1, with the diagram in Figure A.4 indicating where Dim 1 and Dim 2 were measured. Note that the cross-sectional area of uni-axial load cell L1 is not included in the table. The measurement was not taken as the strain gages were on the load cell before the measurements of the cross-sectional area were taken.

$$F = \epsilon EA \tag{A.1}$$

**Table A.1.** Cross-sectional area of the uni-axial load cells

Uni-axial load cell	Dim 1 [mm]	Dim 2 [mm]	Cross-sectional area [m <sup>2</sup> ]
L2	10.37	10.37	0.00010754
L3	10.02	10.40	0.00010421
L4	9.81	9.79	0.00009604
L5	9.77	9.84	0.00009614
L6	9.93	9.82	0.00009751



L7	9.95	9.90	0.00009851
L8	9.73	9.76	0.00009496
L9	9.85	9.86	0.00009712
L10	9.89	9.86	0.00009752
L11	10.01	9.89	0.00009900
L12	9.77	9.77	0.00009545
L13	9.73	9.75	0.00009487

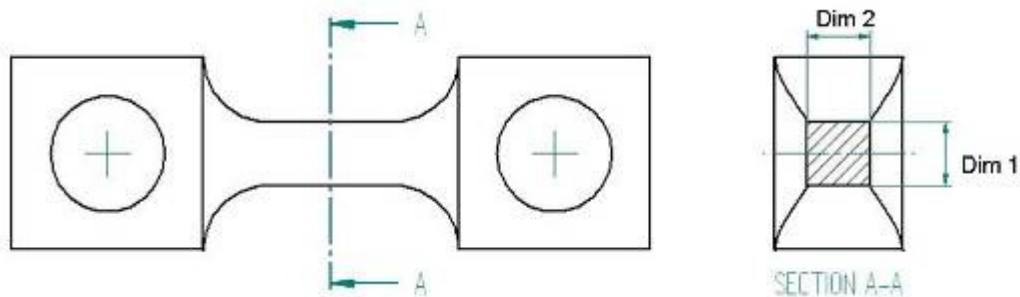


**Figure A.4.** Cross-sectional area of uni-axial load cell

Before the uni-axial load cells were calibrated the tensile strength of the material used to manufacture the uni-axial load cells were measured to make sure that the material used conformed to specification. The permitted force that can be applied without the load cell yielding was calculated using material data. It is important that the uni-axial load cell is not physically deformed as this may cause damage to the strain gages and affect the measurements obtained from the uni-axial load cells. The uni-axial load cells are made of EN19 steel (condition T). A hardness test was performed on two of the uni-axial load cells with four measurements taken on each. The hardness tester used gave the Vickers and Rockwell (C-scale) hardness as output. The Vickers harness (HV) values obtained from the test were converted to Brinell hardness (HB) by means of the ASTM Standard E 140-02 (2002). A test load of 294.2N was used with a dwell time of 5s.

The tensile strength was calculated from the Brinell hardness using Equation {A.2} (Callister, 2003). The results for the hardness test and the calculated tensile strength values are given in Table A.2. For sample 1 a mean tensile strength of 1017.7MPa with a standard deviation of 29.8MPa was obtained and for sample 2 a mean tensile strength of 1116.3MPa with a standard deviation of 26.7MPa was obtained. The mean tensile strengths that were obtained from the tests for the two samples show good agreement to typical tensile strength values of EN19 steel (condition T) (West York Steel, 2009).

$$TensileStrength(MPa) = 3.45 \times HB \quad \{A.2\}$$

**Table A.2.** Results of harness tests

	HV (Vickers hardness)	HRC (Rockwell hardness. C-scale)	HB (Brinell hardness)	Tensile strength [MPa]
Sample 1:				
Measurement 1	304.2	30.2	287.6	992.22
Measurement 2	306.4	30.5	290	1000.5
Measurement 3	311.9	31.2	295.4	1019.13
Measurement 4	323.5	32.6	307	1059.15
Mean				<b>1017.7</b>
Standard deviation				<b>29.8</b>

	HV (Vickers hardness)	HRC (Rockwell hardness. C-scale)	HB (Brinell hardness)	Tensile strength [MPa]
Sample 2:				
Measurement 1	331.6	33.5	315	1086.75
Measurement 2	338.3	34.2	320.6	1106.07
Measurement 3	344.8	34.8	325.4	1122.63
Measurement 4	351.8	35.7	333.3	1149.89
Mean				<b>1116.3</b>
Standard deviation				<b>26.7</b>

Each uni-axial load cell is calibrated separately against a reference load cell. The reference load cell was calibrated against a DH Budenburg dead-weight tester. The uni-axial load cell is placed in series with the reference load cell in a Schenck Hydropulse, as shown in Figure A.5, and calibrated.

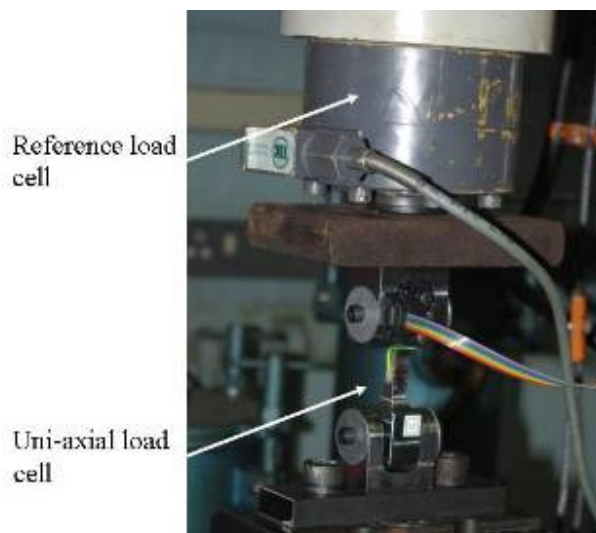


**Figure A.5.** Experimental setup for calibrating the uni-axial load cells

The calibration of the uni-axial load cells were performed by firstly subjecting all of them to a sinusoidal load with an amplitude of 22 300N around a mean of -22 300N and a frequency of 0.5Hz. They were subjected to  $\pm 70$  cycles. This was done as it was initially observed that when the uni-axial load cell was loaded and unloaded for a few cycles an offset between the uni-axial load cell and the reference load cell's force measurement was present (see Figure A.6). This was the case for all the uni-axial load cells. The uni-axial load cells can not be used if they are not able to return to the same initial force value after the loading has been removed. After investigating this phenomenon it was found that after subjecting them to a number of cycles this offset disappeared (see Figure A.7). It was concluded that there might be residual stresses left on the surface of the load cell from manufacturing and after a few cycles of loading and unloading these residual stresses are relieved. For this reason all the load cells were subjected to a cyclic loading in order to relieve these residual stresses. In hindsight it might have been beneficial to anneal the load cells before the strain gages were applied in order to remove residual stresses. However, the method used seems to effectively relieve the residual stresses.

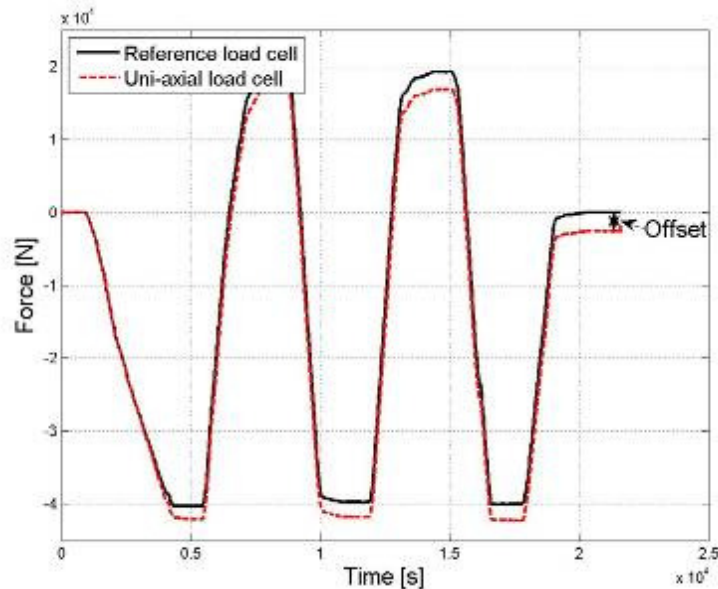


**Figure A.6.** Offset present in uni-axial load cell (Uni-axial load cell L13)

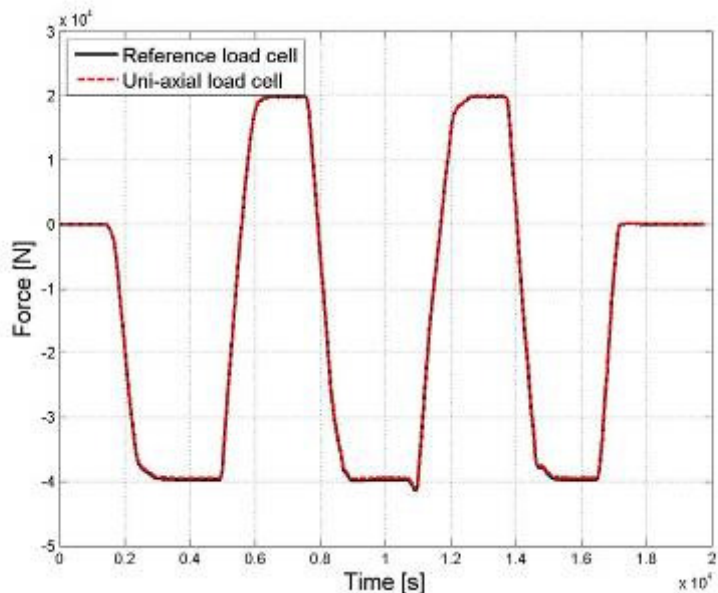


**Figure A.7.** Offset absent after cyclic loading (Uni-axial load cell L13)

After the residual stresses were relieved the uni-axial load cells were given a hand generated input that ranged from  $-39\,639\text{N}$  to  $19819.6\text{N}$ . This signal was used to calibrate the uni-axial load cells. This is also the signal that was used in Figure A.6 and Figure A.7. The uni-axial load cells were calibrated by comparing the force calculated from Eq.{A.1} against the force measured by the reference load cell. The maximum difference between these two signals is then minimized by adjusting the Young's modulus ( $E$ ). The calibrated Young's modulus ( $E$ ) which results in the best correlation between the uni-axial load cell's and reference load cell's force is given in Table A.3. It should be noted that the calibrated Young's modulus takes effects such as the misalignment of the strain-gages into account. The Young's modulus are adjusted as the value for this parameter is more uncertain in this case than the cross-sectional area that was used. Figure A.8 shows the correlation between the calibrated uni-axial load cell's and reference load cell's force measurements using the calibrated values for the Young's modulus. Similar results were obtained for the other twelve load cells. From these results it was concluded that the uni-axial load cells are calibrated and can now be used in the 6clc.

**Table A.3.** Calibrated Young’s modulus

Uni-axial load cell	Calibrated Young’s modulus ( $E$ ) [GPa]
L1	207.09
L2	192
L3	200.41
L4	211.54
L5	211.34
L6	208.4
L7	210
L8	211.5
L9	211
L10	210.4
L12	211
L13	211.35
Mean	208
Standard deviation	5.9

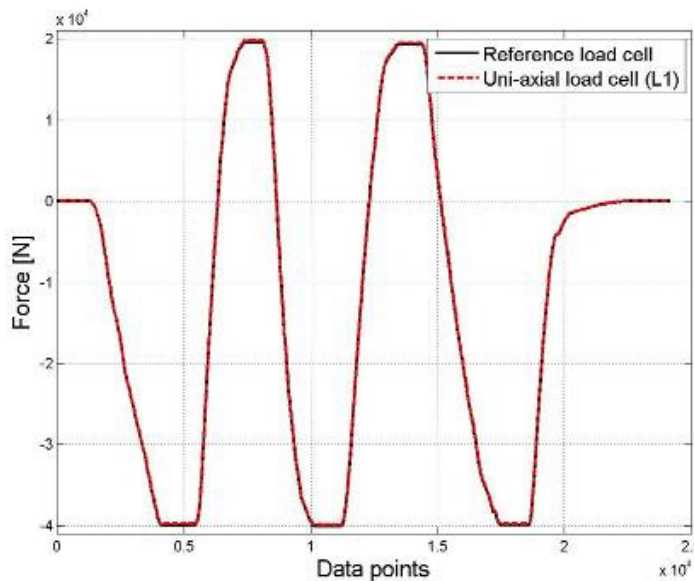


**Figure A.8.** Calibrated uni-axial load cell (L1) compared to reference load cell

## A.2. Verification and Validation of the physical and virtual 6clc

Twelve of the calibrated uni-axial load cells from paragraph A.1 is now incorporated into two 6clcs each using six uni-axial load cells. The two 6clcs will be referred to as the front 6clc and the rear 6clc. Figure A.9 shows the axis system that is used for both the front and rear 6clcs. All measurements and dimensions are relative to the centre of volume (cv) of the 6clc. The verification process will firstly establish whether the concept of the 6clc can indeed work and that it can measure the forces between the chassis and the suspension system. Secondly, the virtual 6clc created in ADAMS/Car will be verified. Analytical equations will be derived in order to verify the concept of the 6clc as well as to verify the ADAMS/Car model. After the concept of the 6clc and the ADAMS/Car model have been verified, both the analytical equations and the ADAMS/Car model will be validated against experimental measurements.



**Figure A.9.** 6clc axis system

Table A.4 shows the four load cases that were used in the verification and validation process. Table A.4 shows the load direction as well as the application point of the applied force relative to the cv of the 6clc for each load case.

**Table A.4.** Load cases used in verification process

	Load direction	Application point	Application point coordinates (Theoretical)
Load case 1	Vertical (negative z-direction)	Center (at the origin of the xy-plane)	[0, 0, 0.085]
Load case 2	Vertical (negative z-direction)	Off center	[0.0475, 0.04, 0.085]
Load case 3	Lateral (y-direction)	Off center	[0.035,-0.0175,0.115]
Load case 4	Longitudinal (negative x-direction)	Off center	[0.0575,-0.0175, 0.101]

### A.2.1. Verification of 6clc

As mentioned, the verification process will establish whether the concept of the 6clc as well as whether the virtual 6clc created in ADAMS/Car is correct. This is done by deriving the equations which calculates the three forces and three moments due to the force applied to the 6clc. The reference point for these forces and moments is the centre of volume (cv) of the 6clc. The three forces and three moments acting at the centre of volume of the 6clc are referred to as the equivalent forces and moments. Similarly, a set of equations are derived to calculate the equivalent forces and moments using the forces in the uni-axial load cells. The results of these two sets of equations are then compared and are expected to give the same results for the equivalent forces and moments. The comparison between these two sets of equations will indicate whether the 6clc is able to measure the equivalent forces and moments correctly and whether the concept of the 6clc is feasible. The equation will also be used to verify the virtual 6clc.

#### A.2.1.1. Derivation of analytical equations

Figure A.10 shows a schematic of the 6clc indicating the position of the applied force which is used in the derivation of the equations. The figure also indicates the position and orientation of the six uni-axial load cells. The equations are derived by considering the free-body diagram of Part 1 in the zy-, zx-, and xy-planes, respectively. Summing the forces in the two directions

and the moments about the third direction for each plane, will result in a set of six equations from which the equivalent forces and moments can be calculated.

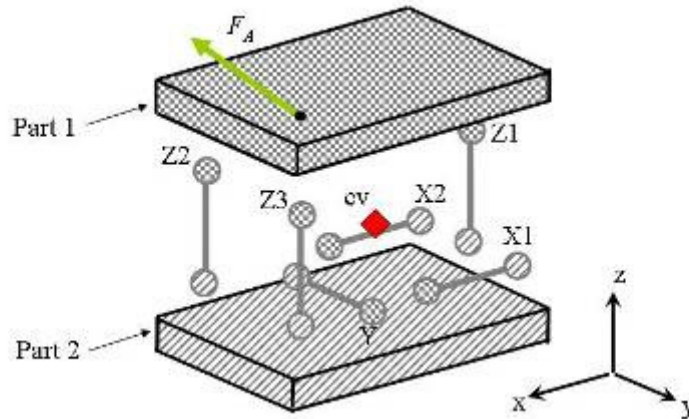


**Figure A.10.** Schematic of 6clc and the six uni-axial load cells it consists of

zy-plane:

Figure A.11 shows the free-body diagram of Part 1 in the zy-plane. Summing the forces in the y- and z-directions and the moment about the x-axis gives the following equations:

$$\begin{aligned} \sum F_z = 0: & \quad Z_1 + Z_2 + Z_3 = F_{Az} \\ \sum F_y = 0: & \quad Y = F_{Ay} \\ \sum M_x = 0: & \quad d_{Yz}Y - d_{Z_2y}Z_2 + d_{Z_3y}Z_3 = d_yF_{Az} - d_zF_{Ay} \end{aligned}$$

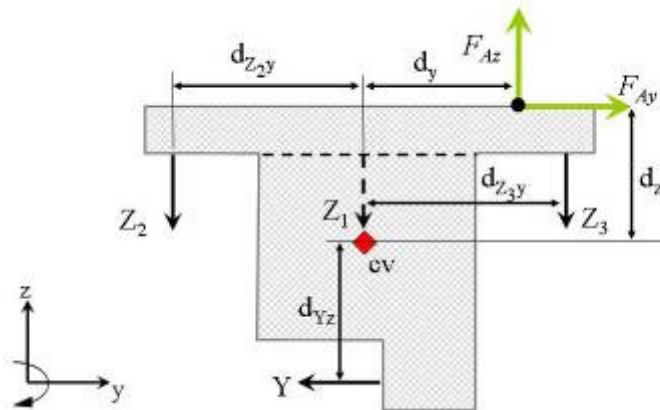


**Figure A.11.** Free body diagram of Part 1 in the zy-plane

zx-plane:

Figure A.12 shows the free-body diagram of Part 1 in the zx-plane. Summing the forces in the x- and z-direction and the moment about the y-axis gives the following equations:

$$\begin{aligned} \sum F_z = 0: & \quad Z_1 + Z_2 + Z_3 = F_{Az} \\ \sum F_x = 0: & \quad X_1 + X_2 = F_{Ax} \\ \sum M_y = 0: & \quad -d_{X_{12z}}(X_1 + X_2) + d_{Z_1x}Z_1 - d_{Z_2x}Z_2 - d_{Z_3x}Z_3 = d_zF_{Ax} - d_xF_{Az} \end{aligned}$$

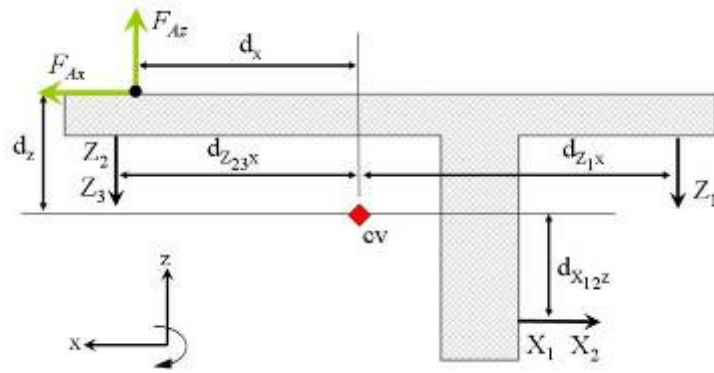


**Figure A.12.** Free body diagram of Part 1 in the  $zx$ -plane

$xy$ -plane

Figure A.13 shows the free-body diagram of Part 1 in the  $xy$ -plane. Summing the forces in the  $x$ - and  $y$ -direction and the moment about the  $z$ -axis gives the following equations:

$$\begin{aligned} \sum F_x = 0: & \quad X_1 + X_2 = F_{Ax} \\ \sum F_y = 0: & \quad Y = F_{Ay} \\ \sum M_z = 0: & \quad -d_{X_1y}X_1 + d_{X_2y}X_2 + d_{Yx}Y = d_xF_{Ay} - d_yF_{Ax} \end{aligned}$$

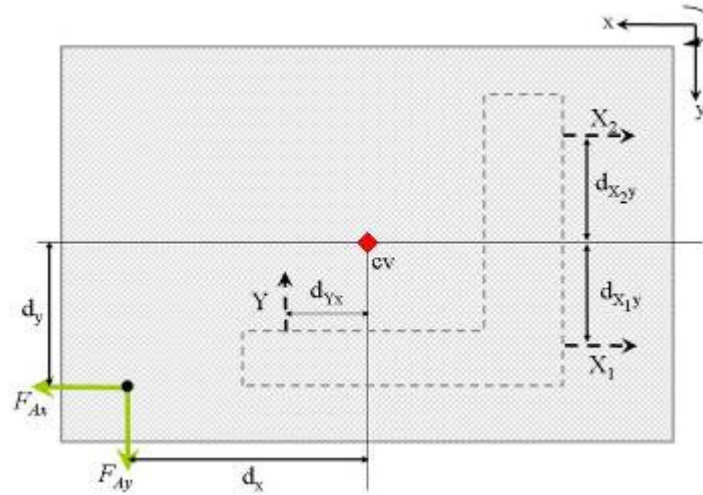


**Figure A.13.** Free-body diagram of Part 1 in the  $xy$ -plane

Combining the forces and moment equations derived from the  $zy$ -,  $zx$ - and  $xy$ -plane the following set of equations are obtained:

$$\begin{aligned} X_1 + X_2 &= F_{Ax} \\ Y &= F_{Ay} \\ Z_1 + Z_2 + Z_3 &= F_{Az} \\ d_{Yz}Y - d_{Z_2y}Z_2 + d_{Z_3y}Z_3 &= d_yF_{Az} - d_zF_{Ay} \\ -d_{X_12z}(X_1 + X_2) + d_{Z_1x}Z_1 - d_{Z_23x}Z_2 - d_{Z_23x}Z_3 &= d_zF_{Ax} - d_xF_{Az} \\ -d_{X_1y}X_1 + d_{X_2y}X_2 + d_{Yx}Y &= d_xF_{Ay} - d_yF_{Ax} \end{aligned} \tag{A.3}$$

The left hand side of the set of equations in Eq.{A.3} is equal to the equivalent forces and moments due to the forces in the uni-axial load cells, whereas, the right hand side is equal to the equivalent forces and moments due to the applied force. It is therefore possible to write the set of equations into two sets calculating either the equivalent forces and moments from the applied force (Eq.{A.4}) or the equivalent forces and moments from the forces in the uni-axial load cells (Eq.{A.5}). The set of equations in Eq.{A.3} can also be used to calculate the forces in the uni-axial load cells due to an applied force (Eq.{A.6}).

#### Equivalent forces and moments calculated from applied force

In order to calculate the equivalent forces and moments from the applied force, Eq.{A.3} is simply rewritten as Eq.{A.4}. The applied force ( $F_A$ ) and its application point ( $d_x, d_y, d_z$ ) relative to the cv is known and the equivalent forces ( $F_x, F_y, F_z$ ) and moments ( $M_x, M_y, M_z$ ) can be calculated.

$$\begin{aligned}
 F_x &= F_{A_x} \\
 F_y &= F_{A_y} \\
 F_z &= F_{A_z} \\
 M_x &= d_y F_{A_z} - d_z F_{A_y} \\
 M_y &= d_z F_{A_x} - d_x F_{A_z} \\
 M_z &= d_x F_{A_y} - d_y F_{A_x}
 \end{aligned} \tag{A.4}$$

#### Equivalent forces and moments calculated from the forces in the uni-axial load cells

In order to calculate the equivalent forces and moments from the forces in the uni-axial load cells, Eq.{A.3} is simply rewritten as Eq.{A.5}. The forces in the uni-axial load cells ( $X_1, X_2, Y, Z_1, Z_2$  and  $Z_3$ ) are known and the equivalent forces ( $F_x, F_y, F_z$ ) and moments ( $M_x, M_y, M_z$ ) can be calculated.

$$\begin{aligned}
 F_x &= X_1 + X_2 \\
 F_y &= Y \\
 F_z &= Z_1 + Z_2 + Z_3 \\
 M_x &= d_{y_z} Y - d_{z_2_y} Z_2 + d_{z_3_y} Z_3 \\
 M_y &= -d_{x_{12_z}} (X_1 + X_2) + d_{z_1_x} Z_1 - d_{z_2 z_3_x} (Z_2 + Z_3) \\
 M_z &= -d_{x_{1_y}} X_1 + d_{x_{2_y}} X_2 + d_{y_x} Y
 \end{aligned} \tag{A.5}$$

#### Calculate force in uni-axial load cells due to applied force

The set of equations in Eq.{A.3} can be written in matrix form  $Ax = b$ , as shown in Eq.{A.6}.



$$\begin{bmatrix} 1 & 1 & 0 & 0 & 0 & 0 \\ 0 & 0 & 1 & 0 & 0 & 0 \\ 0 & 0 & 0 & 1 & 1 & 1 \\ 0 & 0 & d_{Yz} & 0 & -d_{Z2y} & d_{Z3y} \\ -d_{X12z} & -d_{X12z} & 0 & d_{Z1x} & -d_{Z23x} & -d_{Z23x} \\ -d_{X1y} & d_{X2y} & d_{Yx} & 0 & 0 & 0 \end{bmatrix} \begin{Bmatrix} X_1 \\ X_2 \\ Y \\ Z_1 \\ Z_2 \\ Z_3 \end{Bmatrix} = \begin{Bmatrix} F_{Ax} \\ F_{Ay} \\ F_{Az} \\ d_y F_{Az} - d_z F_{Ay} \\ d_z F_{Ax} - d_x F_{Az} \\ d_x F_{Ay} - d_y F_{Ax} \end{Bmatrix} \quad \{A.6\}$$

Substituting  $d_{X1y} = d_{X2y} = d_{Z2y} = d_{Z3y}$  with  $d_1$

$$d_{Yx} = d_{X12z} = d_{Yz} \text{ with } d_2$$

$$d_{Z1x} = d_{Z23x} \text{ with } d_3$$

we can rewrite matrix A as follows:

$$A = \begin{bmatrix} 1 & 1 & 0 & 0 & 0 & 0 \\ 0 & 0 & 1 & 0 & 0 & 0 \\ 0 & 0 & 0 & 1 & 1 & 1 \\ 0 & 0 & d_2 & 0 & -d_1 & d_1 \\ -d_2 & -d_2 & 0 & d_3 & -d_3 & -d_3 \\ -d_1 & d_1 & d_2 & 0 & 0 & 0 \end{bmatrix}$$

The values for  $d_1$ ,  $d_2$  and  $d_3$  are obtained from the dimensions of the 6clc. Substituting the values of  $d_1=0.045m$ ,  $d_2=0.035m$  and  $d_3=0.0825m$  into matrix A the determinant of the matrix can be calculated. The  $\det(A) = 0.0013$  and implies that the system of linear equations has a unique solution because  $\det(A) \neq 0$ . This implies that Eq.{A.3} rewritten in the form of Eq.{A.6} can be used to calculate the forces in the uni-axial load cells due to the applied force.

#### A.2.1.2. Verification of 6clc concept

Comparing the results from Eq.{A.4} and Eq.{A.5} we can verify whether the 6clc can indeed measure the equivalent forces and moments correctly. Figure A.14 shows the results obtained from Eq.{A.4} and Eq.{A.5} when a force ( $F_A$ )<sup>1</sup> is applied to the 6clc. This figure shows that Eq.{A.4} and Eq.{A.5} does indeed give the same answers and implies that the concept is feasible. It should be noted that in order to get the results in Figure A.14 the force in the uni-axial load cells ( $X_1$ ,  $X_2$ ,  $Y$ ,  $Z_1$ ,  $Z_2$  and  $Z_3$ ), used in Eq.{A.5}, was obtained from solving Eq.{A.6}. Note that both Eq.{A.4} and Eq.{A.6} uses the applied force ( $F_A$ ) and its associated coordinates ( $d_x$ ,  $d_y$  and  $d_z$ ). This may lead to errors in the equations being disguised as the inputs equal the outputs, and vice versa. The second part of the verification procedure may help to identify problems with the equations. A model of the 6clc is created in ADAMS/Car. The same applied force<sup>1</sup> used to generate the results in Figure A.14 will be applied to the ADAMS/Car model. The reaction forces measured by the ADAMS/Car model will then be substituted into Eq.{A.5} in order to calculate the equivalent forces and moments that can be compared with the results of Eq.{A.4}. If the comparisons show good correlation

<sup>1</sup> For this example the applied force had the following characteristic:  $F_{Ax} = 200 \sin(2\pi ft)$  N,

$F_{Ay} = 150 \sin(2\pi ft)$  N and  $F_{Az} = 2000 \sin(2\pi ft)$  N. Applied at [0m, 0.001m, 0.085m].

then we will consider the analytical equations and the ADAMS/Car model, of the 6clc, verified. The next step will then be to validate the results from the analytical equations and the ADAMS/Car model against experimental measurements.

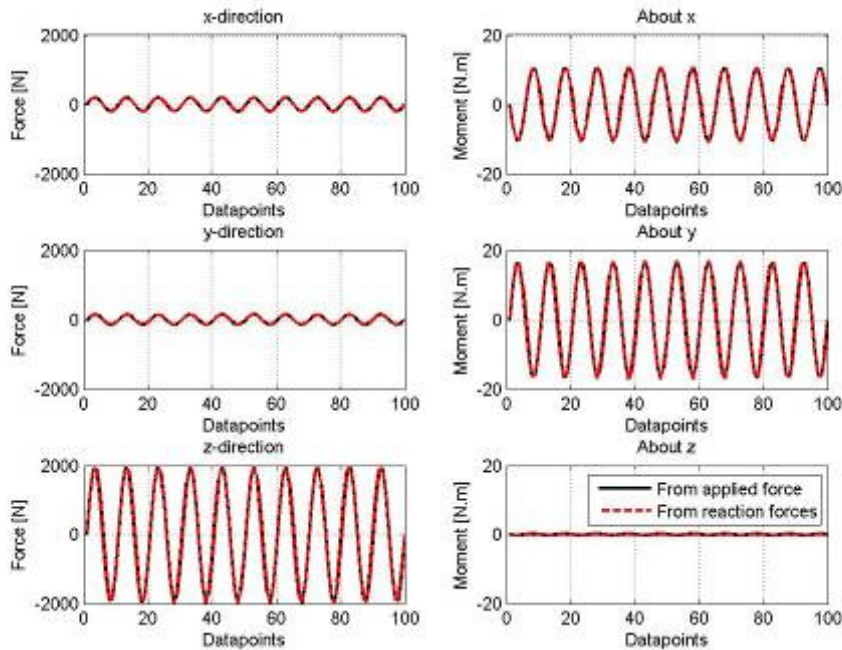


**Figure A.14.** Compare results from Eq. {A.4} and Eq. {A.5}

### A.2.1.3. Verification of the 6clc ADAMS/Car model

This paragraph considers the verification of the ADAMS/Car model. The 6clc that is modelled in ADAMS/Car consists of:

- 15 Moving Parts (not including ground)
- 1 Cylindrical Joint
- 6 Spherical Joints
- 6 Translational Joints
- 6 Constant velocity Joints
- 1 Fixed Joint
- 1 Inplane Primitive Joint
- 7 Motions

The 6clc model has zero degrees of freedom. Figure A.15 shows the ADAMS/Car model of the 6clc. The force is applied to the 6clc model via three point-point actuators each representing the three components of the applied force. Each component can be given a specified force. The 6clc model measures the forces in the uni-axial load cells through the translational joints that are used to connect the two bodies representing the uni-axial load cells. The two bodies are connected to the two parts of the 6clc via a spherical joint at the one end and a constant velocity joint at the other end.

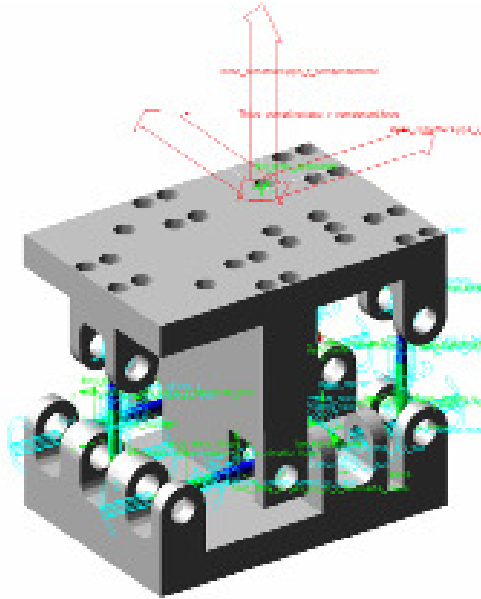


**Figure A.15.** ADAMS/Car model of 6clc

Before the 6clc model is subjected to the load cases that were shown in Table A.4 the ADAMS/Car model was analysed with no external force applied to it. The results obtained from the analytical equations and the ADAMS/Car model is shown in Table A.5. As expected the results of the analytical equations are zero for the force in the uni-axial load cells and for the equivalent forces and moments. The forces in the uni-axial load cell in the ADAMS/Car models, however, have non-zero values and therefore give non-zero values for the equivalent forces and moments. This difference is due to the mass of the two parts not being included in the analytical equation, whereas in the ADAMS/Car model the mass was included. It is expected that when the 6clc load cell is orientated such that the gravitational field acts in the negative z-direction, and has no force applied to it, that  $X_1$ ,  $X_2$ ,  $Y$ ,  $F_x$ ,  $F_y$  and  $M_z$  should be zero, but Table A.5 indicates that this is not the case. The non-zero values of these parameters are merely a result of the centre of mass of the 6clc not going through the centre of volume. The values for the forces in the uni-axial load cells shown in Table A.5 for the ADAMS/Car model will be subtracted from the ADAMS/Car measurements for  $X_1$ ,  $X_2$ ,  $Y$ ,  $Z_1$ ,  $Z_2$  and  $Z_3$ . This is done as the measurements of  $X_1$ ,  $X_2$ ,  $Y$ ,  $Z_1$ ,  $Z_2$  and  $Z_3$  in the physical 6clc load cell was zeroed when under its own mass.

**Table A.5.** Results from analysis with no load applied to 6clc

	<b>Analytical</b> Eq.{A.4} and Eq.{A.5} [N]	<b>ADAMS/Car model</b> [N]
<b>Forces in uni-axial load cells</b>		
$X_1$	0	1.6439e-007
$X_2$	0	-2.1334e-007
$Y$	0	2.5271e-007
$Z_1$	0	-42.1146
$Z_2$	0	-18.147
$Z_3$	0	-25.0167
<b>Equivalent forces</b>		
$F_x$	0	-4.8946e-008
$F_y$	0	2.5271e-007
$F_z$	0	-85.2783

	<b>Analytical</b> Eq. {A.4} and Eq. {A.5} [N]	<b>ADAMS/Car model</b> [N]
<b>Equivalent moments</b>		
$M_x$	0	-0.30914
$M_y$	0	0.086554
$M_z$	0	-8.1529e-009

Using Load case 1, we will check whether cross-sensitivity between the uni-axial load cells in the three directions exists. With Load case 1,  $X_1$ ,  $X_2$ ,  $Y$ ,  $F_x$ ,  $F_y$  and  $M_z$  is expected to be zero. The results from the analytical equations are indeed zero for  $X_1$ ,  $X_2$ ,  $Y$ ,  $F_x$ ,  $F_y$  and  $M_z$  whereas the results from the ADAMS/Car model is not. Table A.6 shows the maximum difference between the analytical and ADAMS/Car results.

From the results in Table A.6 it can be seen that as the magnitude of the vertical component of the applied force is changed the difference between the analytical and ADAMS/Car results become larger. This seems to indicate that there exists a small amount of cross-sensitivity of the uni-axial load cells in the different directions. However, the force present in the uni-axial load cells due to the cross-sensitivity is very small and will have a negligible effect on the accuracy of the 6clc model's measurements.

**Table A.6.** Maximum difference between analytical results and ADAMS/Car results (Load case 1)

	<b>Load case 1</b> ( $F_z = -100\text{N}$ )	<b>Load case 1</b> ( $F_z = -1000\text{N}$ )	<b>Load case 1</b> ( $F_z = -10000\text{N}$ )
<b>Forces in uni-axial load cells</b>			
$X_1$	2.226e-7	2.226e-6	2.226e-5
$X_2$	3.727e-7	3.727e-6	3.727e-5
$Y$	4.673e-7	4.673e-6	4.673e-5
$Z_1$	3.173e-6	3.173e-6	5.098e-6
$Z_2$	5.17e-7	4.13e-6	4.595e-5
$Z_3$	3.304e-5	3.65e-5	7.085e-5
<b>Equivalent forces</b>			
$F_x$	1.5e-7	1.5e-6	1.5e-5
$F_y$	4.673e-7	4.673e-6	4.673e-5
$F_z$	3e-5	3e-5	3e-5
<b>Equivalent moments</b>			
$M_x$	1.468e-6	1.664e-6	3.621e-6
$M_y$	3e-6	3e-6	3e-6
$M_z$	1.043e-8	1.043e-7	1.043e-6

The analytical equations and the ADAMS/Car model are subjected to load cases 2 to 4 with the non-zero components of the applied force having the characteristic shown in Figure A.16. It is a ramp input with maximum amplitude of -4000N. The results for the different load cases are shown in Table A.7.

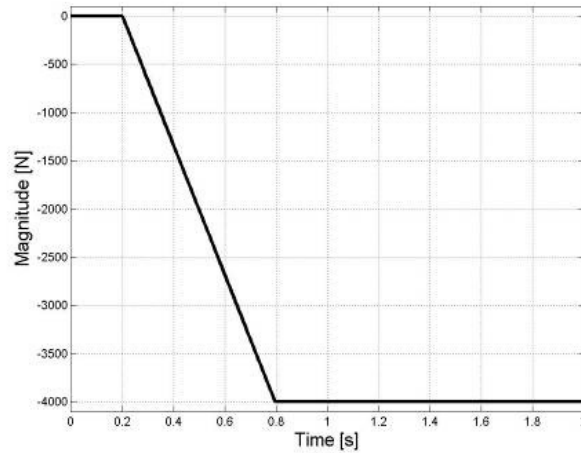


**Figure A.16.** Characteristic of the components of the applied force

**Table A.7.** Maximum difference between analytical results and ADAMS/Car results (Load case 2 to 4)

	<b>Load case 2</b> $F_x = 0\text{N}$ $F_y = 0\text{N}$ $F_z = -4000\text{N}$	<b>Load case 3</b> $F_x = 0\text{N}$ $F_y = -4000\text{N}$ $F_z = 0\text{N}$	<b>Load case 4</b> $F_x = -4000\text{N}$ $F_y = 0\text{N}$ $F_z = 0\text{N}$	$F_x = -4000\text{N}$ $F_y = -4000\text{N}$ $F_z = -4000\text{N}$ (Same application point as Load case 2)
<b>Forces in uni-axial load cells</b>				
$X_1$	2.158e-6	2.551e-6	3.4e-5	3.47e-5
$X_2$	8.076e-8	1.416e-5	3.177e-5	4.5e-5
$Y$	1.377e-5	4.76e-6	2.612e-5	3.52e-5
$Z_1$	3.173e-6	3.173e-6	7.2e-6	9.5e-6
$Z_2$	7.837e-6	6.57e-6	1.2e-5	1.26e-5
$Z_3$	3.99e-5	3.27e-5	3.77e-5	3.3e-5
<b>Equivalent forces</b>				
$F_x$	2.239e-6	1.671e-5	2.29e-6	1.026e-5
$F_y$	1.377e-5	4.76e-6	2.612e-5	3.52e-5
$F_z$	3e-5	3e-5	3e-5	3e-5
<b>Equivalent moments</b>				
$M_x$	1.67e-6	1.65e-6	1.446e-6	1.446e-6
$M_y$	3e-6	3e-6	3e-6	3e-6
$M_z$	5.754e-7	6.89e-7	2.05e-6	2.35e-6

From the results shown in Table A.6 and Table A.7 it can be concluded that the ADAMS/Car model was constructed correctly and is able to measure the equivalent forces and moments applied to the virtual 6clc. The ADAMS/Car model as well as the analytical equations will now be validated against experimental results. This is done as comparing the results of the two models with one another only verifies that the models have been created correctly, but does not indicate whether either model is correct and can measure the force in the uni-axial load cells correctly, and infer the equivalent forces and moments. In the following paragraph we will discuss the validation of the 6clc models.

### A.2.2. Validation of 6clc models

The 6clc ADAMS/Car model has been verified. The next step before the 6clc model can be used is to validate it. The validation will consist of qualitatively comparing the measurements of the physical 6clc and the “measurements” of the 6clc ADAMS/Car model. The analytical

equations will also be compared to the measurements of the physical 6clc measurements. In the comparisons the data referred to as the **Measured** data is obtained from the physical 6clc measurements. The forces in the uni-axial load cells (i.e.  $X_1$ ,  $X_2$ ,  $Y$ ,  $Z_1$ ,  $Z_2$  and  $Z_3$ ) are obtained by taking the strain measurements of each uni-axial load cell and then using Eq.{A.2} to calculate the force. Once the measured force in each of the uni-axial load cells have been calculated Eq.{A.5} is used to calculate the equivalent forces and moments. The **Analytical** data refers to the data obtained by calculating the uni-axial load cell forces and the equivalent forces and moments due to the applied force. The forces in the uni-axial load cells are calculated using Eq.{A.6} and the equivalent forces and moments are calculated using Eq.{A.4}. The last set of data used in the comparisons is the data from the 6clc ADAMS/Car model which will be referred to as **acar**. The uni-axial load cells in the ADAMS/Car model was modelled such that the force measured by the uni-axial load cells is already in Newtons. Therefore, the uni-axial load cell forces obtained from the ADAMS/Car model can directly be substituted into Eq.{A.5} to calculate the equivalent forces and moments.

The experimental setup that was used to obtain the experimental data required for the validation process is shown in Figure A.17. An external force is applied to the 6clc via the actuator which will be referred to as the applied force. The force is applied to the actuator at a known location for the different load cases as was given in Table A.4. The applied force is measured by the load cell. The measured applied force is used in the analytical equations as well as applied to the ADAMS/Car model. The same load cases are used that was used in the verification process (see Table A.4). The validation results of the 6clc models for each of the load cases is given in the following paragraphs.

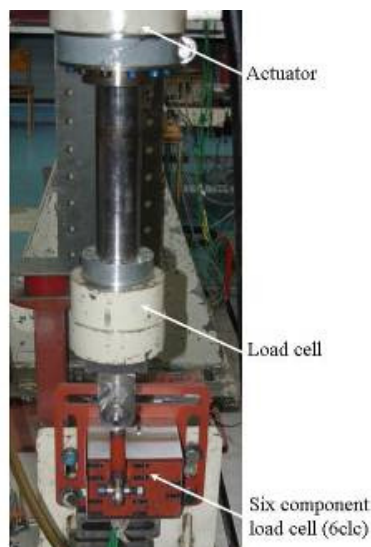
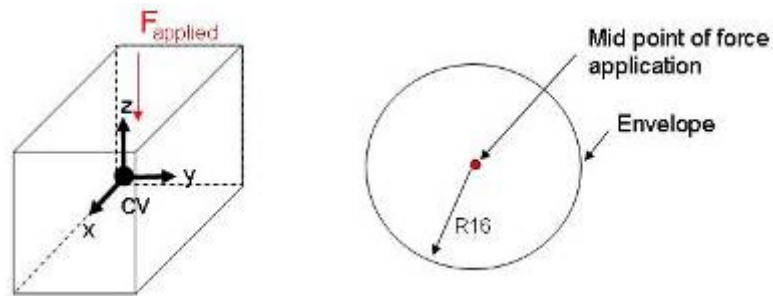


**Figure A.17.** Experimental setup of 6clc for Load case 3

#### A.2.2.1. Load case 1 and Load case 2

The force in the vertical direction was applied both at the origin of the xy-plane (Load case 1) as well as at an off-centre location (Load case 2). The interface between the actuator and the 6clc was a 32mm round tube that transferred the load to the 6clc. The midpoint of the round tube corresponded with the application point given in Table A.4. This assumed that the load, applied through the 32mm round tube, will be a perfect point load and that it will act at the mid point of the tube at the specified location. However, in the experimental setup it may happen that the load is actually applied at some other point within the circular envelope formed by the round tube (see Figure A.18). This implies that it may happen that the practical

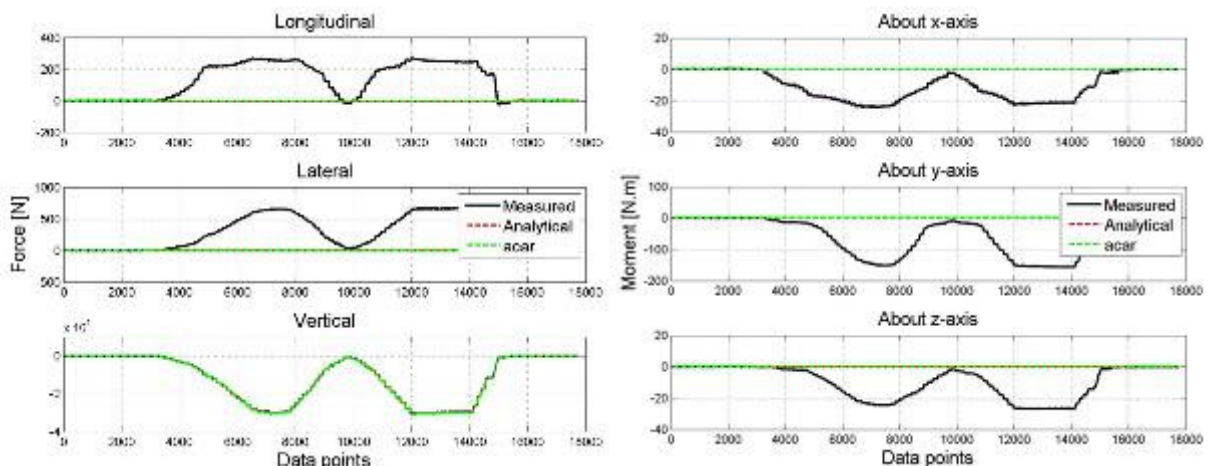
application points differ from the theoretical application points and thus influence the results of the equivalent moments and forces calculated by Eq. {A.4}.



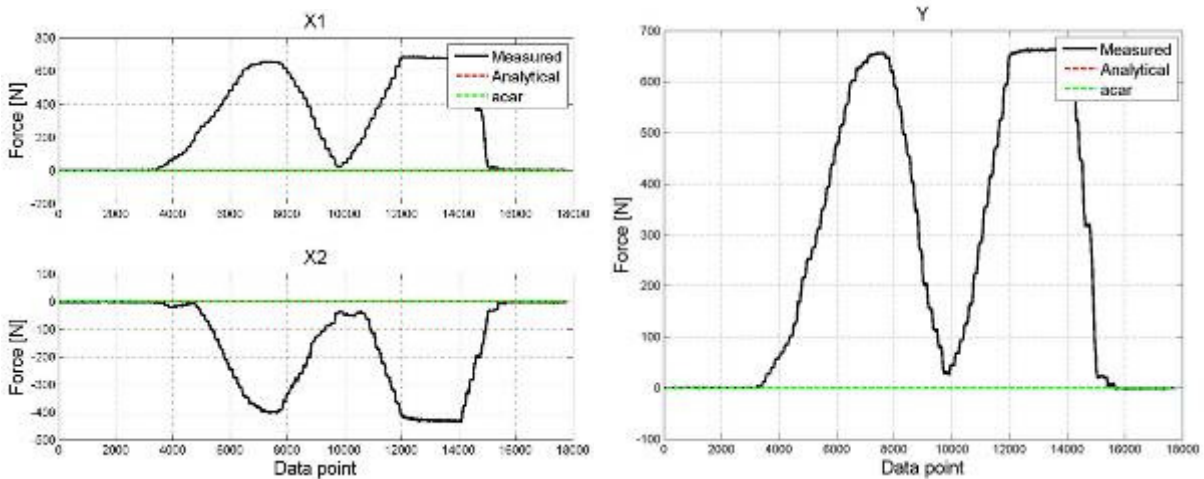
**Figure A.18.** Force application for Load case 1 and 2

Figure A.19 shows the comparison of the equivalent forces and moments between the two models and the physical 6clc when subjected to Load case 1. From this figure it can be observed that the equivalent vertical force measured on the physical 6clc and the two models show good agreement. However for the other two forces and all three moments there is not good agreement. It is difficult to distinguish between the results from the two models (Analytical and acar) in Figure A.19. This is because the results are equal. Figure A.20 and Figure A.21 show the correlation of the forces in the six uni-axial load cells. As can be expected for this load case the analytical equations and the ADAMS/Car model measures no forces in the lateral and longitudinal directions (see Figure A.20). The physical 6clc, however, does measure forces in the uni-axial load cells  $X_1$ ,  $X_2$  and  $Y$ . The forces present in  $X_1$ ,  $X_2$  and  $Y$  of the physical 6clc but which are not measured in the 6clc models, cause the deviation observed in the equivalent forces and moments.

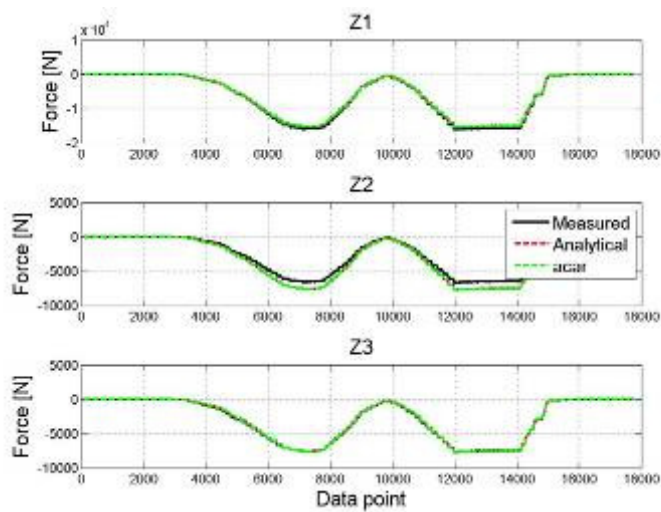
From Figure A.19 it would seem that the two models measure the vertical force correctly, however, when the forces in the uni-axial load cells in the  $z$  direction are viewed (see Figure A.21) it can be observed that there is some deviation between the measured and predicted forces in the uni-axial load cells.



**Figure A.19.** Comparison of equivalent forces and moments (Load case 1)



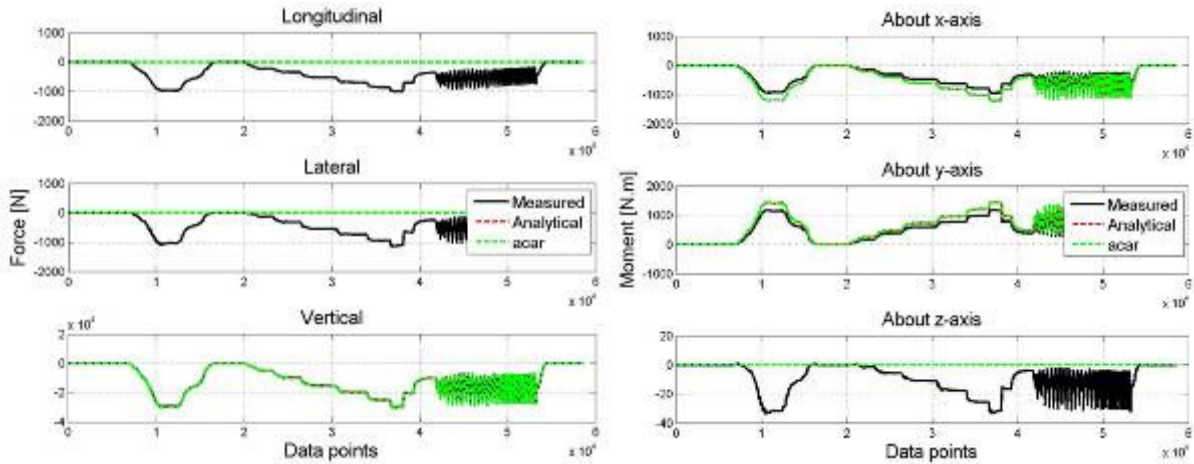
**Figure A.20.** Comparison of forces in uni-axial load cells orientated in the longitudinal and lateral direction (Load case 1)



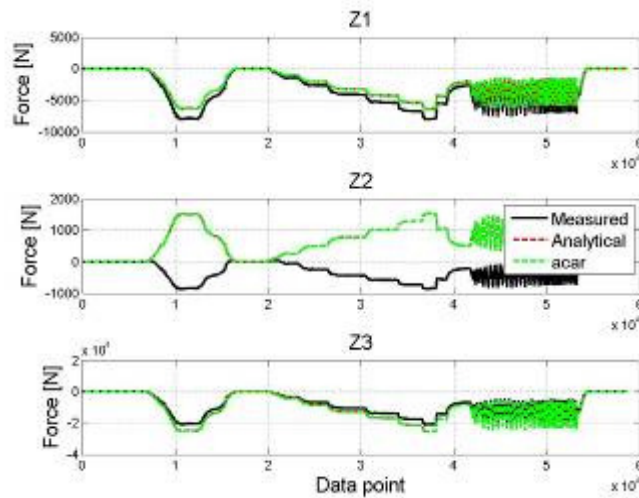
**Figure A.21.** Comparison of forces in uni-axial load cells orientated in vertical direction (Load case 1)

Figure A.22 shows the comparison of the equivalent forces and moments when the 6clc is subjected to Load case 2. It can be observed that the predicted equivalent vertical force from the two models has good correlation with the measured data. The equivalent moment around the x- and y-axis also shows good correlation. Once again the forces in the uni-axial load cells measured by the two models in the longitudinal and lateral direction are zero. Similar to the results obtained for Load case 1, the results show that the equivalent vertical force has good correlation between measured and predicted data, however, this is not true for the forces in the uni-axial load cells orientated in the z-direction, especially for  $Z_2$ . This is shown in Figure A.23.





**Figure A.22.** Comparison of equivalent forces and moments (Load case 2)



**Figure A.23.** Comparison of forces in uni-axial load cells orientated in the vertical direction (Load case 2)

A.2.2.2. Load case 3

In this load case the force is applied to the 6clc via a spherical joint and yoke. Figure A.24 shows the experimental setup and a schematic of the 6clc showing the orientation of the applied force in the 6clc's coordinate system.

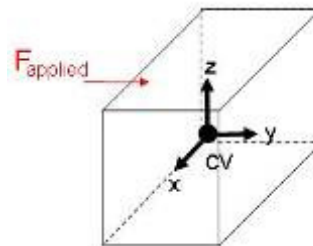


**Figure A.24.** Experimental setup for Load case 3

The equivalent lateral force and the moments about the x- and z-axis show good correlation between the measured and model data (see Figure A.25). The moment about the z-axis uses the forces in the uni-axial load cells  $X_1$ ,  $X_2$  and  $Y$ . It is interesting to note that the comparison of the results from the two models and the measured force in the uni-axial load cell  $Y$  shows good correlation whereas  $X_1$  and  $X_2$  do not show good correlation as shown in Figure A.26. Even though the models do not give good predictions of  $X_1$  and  $X_2$ , good correlation is still obtained for the moment about the z-axis. This is most likely due to the models giving accurate measurements for  $Y$  and with the forces in  $Y$  being much higher than in  $X_1$  and  $X_2$ .

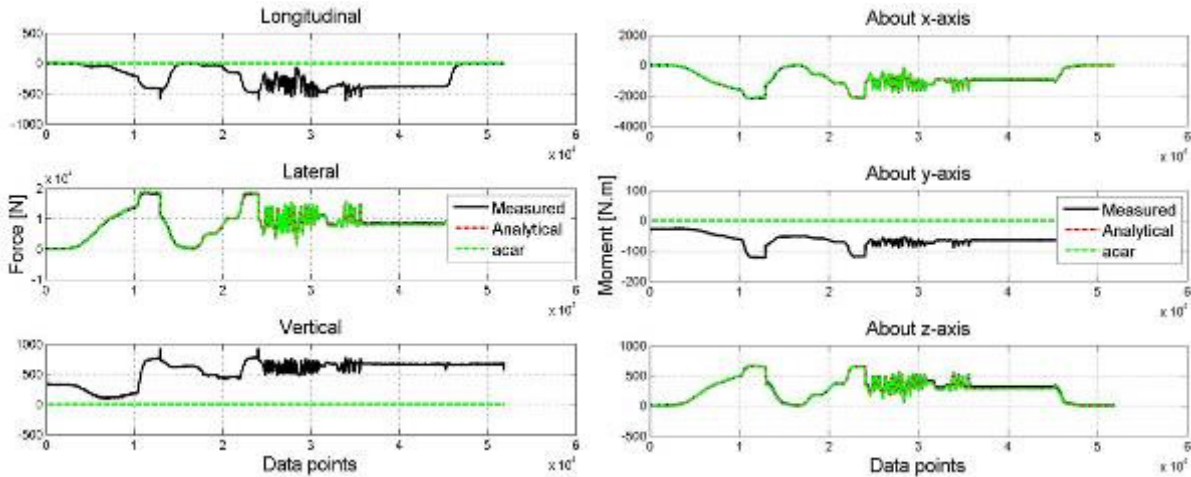


Figure A.25. Comparison of equivalent forces and moments (Load case 3)

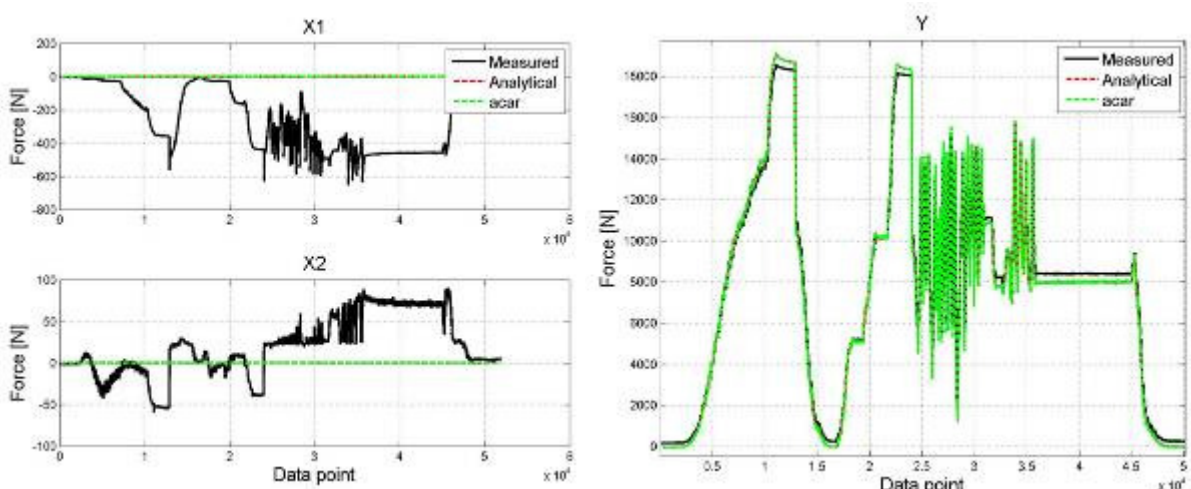
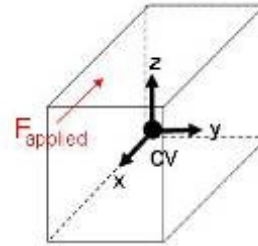


Figure A.26. Comparison of forces in uni-axial load cells orientated in the longitudinal direction (Load case 3)

#### A.2.2.3. Load case 4

In this load case the force is applied to the side of the yoke, which is attached to the 6clc, through the same 32mm tube that was used in Load case 1 and Load case 2. The experimental setup and a schematic of the 6clc showing the orientation of the applied force ( $F_{applied}$ ) in the 6clc's coordinate system are shown in Figure A.27. Because the loading is applied through the 32mm round tube the same effect as described in Load case 1 and 2 can occur here.



**Figure A.27.** Experimental setup for Load case 4

The equivalent longitudinal force and the moments about the y- and z-axis show good correlation between the measured and the results from the two models, as shown in Figure A.28. The moment about the z-axis uses the forces in the uni-axial load cells  $X_1$ ,  $X_2$  and  $Y$ . The uni-axial load cell forces in  $X_1$  and  $X_2$  shows much better correlation between the measured and the models' results than the uni-axial load cell  $Y$ 's forces as shown in Figure A.29. Similar to what was observed in Load case 3, the models' prediction of the equivalent moment about the z-axis is good inspite of the deviation in their prediction of the uni-axial load cell  $Y$ 's force from the measured data. This is due to the good correlation of the models' forces in  $X_1$  and  $X_2$  and the higher forces present in  $X_1$  and  $X_2$  compared to the forces in  $Y$ .

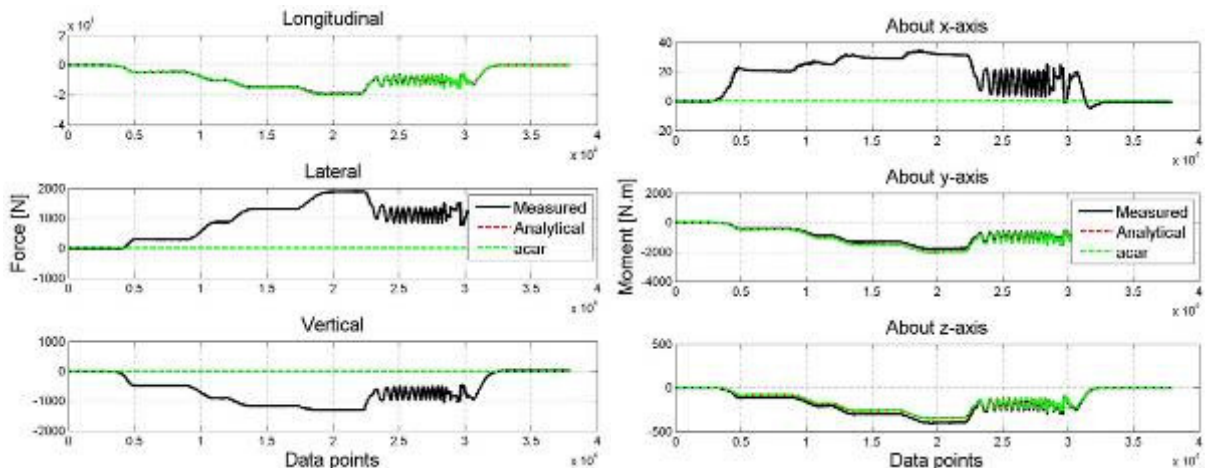


**Figure A.28.** Comparison of equivalent forces and moments (Load case 4)

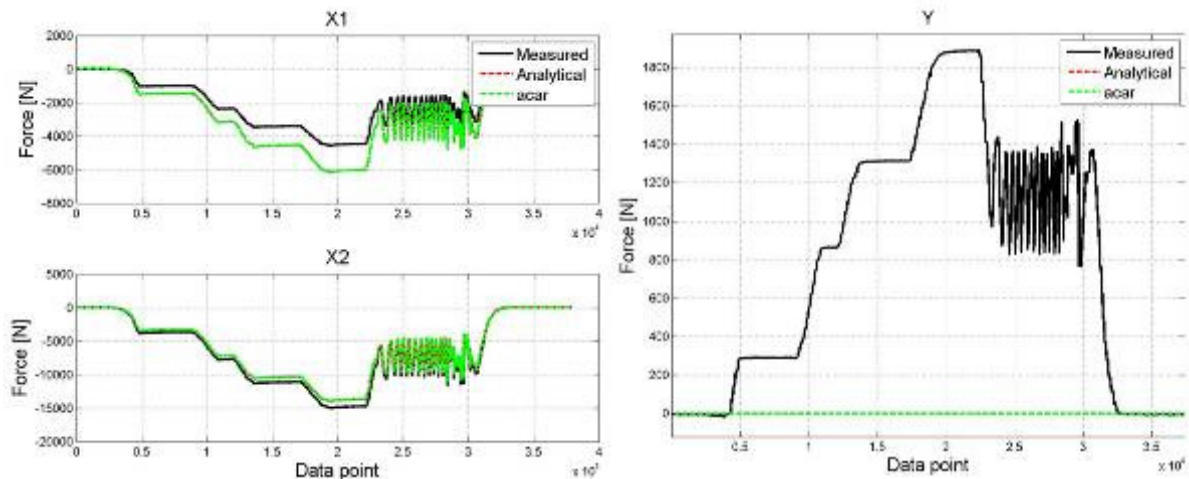


**Figure A.29.** Comparison of forces in uni-axial load cell orientated in the longitudinal and lateral direction (Load case 4)

It was observed in the previous paragraphs that for each load case good correlation was obtained for one of the equivalent forces and for two of the equivalent moments. For the other two equivalent forces and moment the analytical equations and ADAMS/Car model's measurements did not correlate well. It was mentioned that in some of the load cases the theoretical force application point may not actually coincide with the practical application point. This was mainly as a result of how the force was applied to the physical 6clc. This possible cause, along with three other possible causes, are listed below. One, or a combination of them, might be the cause for the deviation observed:

- The practical application point may differ from the theoretical application point
- The applied force may not be purely in one direction but might have another orientation,
- The physical 6clc had some play between the rod end of the uni-axial load cells and the bolts,
- The physical 6clc is not perfectly rigid whereas the models are.

### A.2.3. Model refinement

From the validation results shown in paragraph A.2.2 it was concluded that four possible causes may be responsible for the deviation between the results of the equivalent forces and moments as well as the forces in the uni-axial load cells obtained from the physical 6clc and the two models. In this paragraph the two most likely causes will be investigated namely, the force orientation and the force application point.

In order to investigate the effect of the force orientation and its application point on the results, the orientation of the force as well as its application point will be calculated from the experimentally measured forces in the uni-axial load cells. After the orientation of the forces and its application point have been calculated from the experimental measurements, it will be used in the two models. This should improve the correlation as the physical and virtual 6clc should then be subjected to the same conditions. Considering Equation {A.3}, presented here for convenience as Eq.{A.7}, the left hand side of the equations contain the components of the applied force as well as the coordinates of its application point. The right hand side of the equations contain the forces in the uni-axial load cells as well as their location relative to the centre of volume.

$$\begin{aligned}
 F_{A_x} &= X_1 + X_2 \\
 F_{A_y} &= Y \\
 F_{A_z} &= Z_1 + Z_2 + Z_3 \\
 d_y F_{A_z} - d_z F_{A_y} &= d_{yz} Y - d_{z2y} Z_2 + d_{z3y} Z_3 \\
 d_z F_{A_x} - d_x F_{A_z} &= -d_{x1z} (X_1 + X_2) + d_{z1x} Z_1 - d_{z23x} (Z_2 + Z_3) \\
 d_x F_{A_y} - d_y F_{A_x} &= -d_{x1y} X_1 + d_{x2y} X_2 + d_{yx} Y
 \end{aligned}
 \tag{A.7}$$

All the values on the right hand side are known and it should therefore be possible to calculate the components and the application point of the applied force from the experimental measurements of the forces in the uni-axial load cells. The set of equations in Eq.{A.7} are unfortunately not linear independent. However, dividing the set of equations in Eq.{A.7} into two sets of equations consisting of the three forces and the three moment equations we can

solve for the three components of the applied force ( $F_{Ax}$ ,  $F_{Ay}$ ,  $F_{Az}$ ) as well as its coordinates ( $d_x$ ,  $d_y$ ,  $d_z$ ) as discussed in the following two paragraphs. Paragraph A.2.3.1 discusses the results when the experimentally calculated orientation of the applied force is used in the two models and paragraph A.2.3.2 discusses the results when the experimentally calculated application point is used.

### A.2.3.1. Orientation of applied force

The components of the applied force are calculated from the experimental force measurements in the uni-axial load cells ( $X_1$ ,  $X_2$ ,  $Y$ ,  $Z_1$ ,  $Z_2$  and  $Z_3$ ) using the three force equations in Eq.{A.7} shown here as Eq.{A.8}.

$$\begin{aligned} F_{A_x} &= X_1 + X_2 \\ F_{A_y} &= Y \\ F_{A_z} &= Z_1 + Z_2 + Z_3 \end{aligned} \quad \text{[A.8]}$$

The three components of the applied force, and therefore the orientation of the applied force, can easily be calculated using Eq.{A.8}. Using the experimentally calculated applied force orientation for Load case 1 in the analytical equations and the ADAMS/Car model gives the results shown in Figure A.30. An improvement in the correlation of the longitudinal and lateral equivalent forces can be seen from Figure A.30. The equivalent moments do not however show any improvement in the correlation between the data of the two models and the measured data. Unlike the results for Load case 1 shown in Figure A.30, the correlation between the results for Load case 3 shows great improvements for both the equivalent forces as well as the equivalent moments (see Figure A.31).

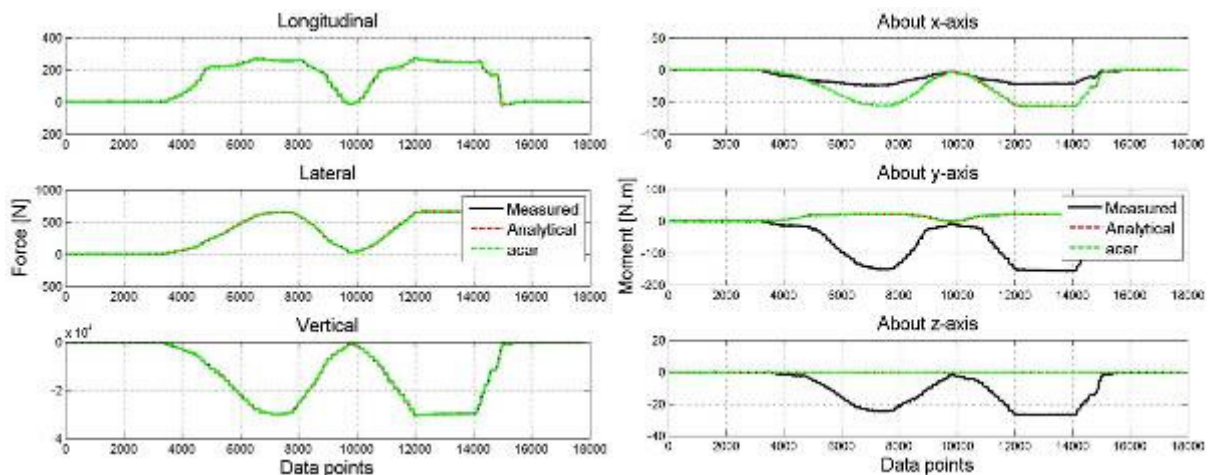


**Figure A.30.** Comparison of equivalent forces and moments (Load case 1 – Experimental loading)

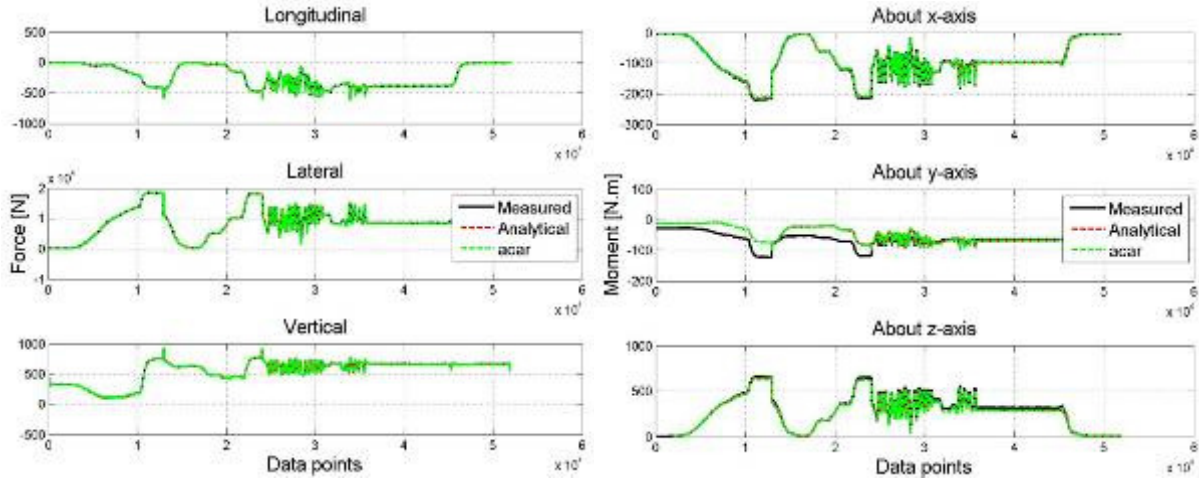


**Figure A.31.** Comparison of equivalent forces and moments (Load case 3 – Experimental loading)

The possibility that the orientation of the applied force between the physical 6clc and the two models differ was investigated. The components of the applied force were calculated from the experimental measurements of the force in the uni-axial load cells in the physical 6clc and were used as input to the analytical equations and the ADAMS/Car model. This showed improvement in the correlation of the equivalent forces for both Load case 1 and Load case 3. Improvement in the correlation of the equivalent moments was obtained only for Load case 3. The fact that good correlation is obtained for the equivalent forces but not for the equivalent moments seem to indicate that there might be an error in the application point of the applied force. This is investigated in the next paragraph.

#### A.2.3.2. Application point of applied force

In the previous paragraph the orientation of the applied force was calculated from experimental measurements. When this force orientation was used in the two models an improvement in the comparisons was observed. The effect of the application point on the correlation is now checked by calculating the application point from the experimental measurements and using these coordinates in the two models. The application point will be calculated using the three moment equations in Eq.{A.7} shown here as Eq.{A.9}. The three components of the applied force ( $F_{Ax}$ ,  $F_{Ay}$ ,  $F_{Az}$ ) in Eq.{A.9} can be calculated using Eq.{A.8}. Eq.{A.9} therefore results in a set of three linear equations with three unknowns.

$$\begin{aligned}
 d_y F_{Az} - d_z F_{Ay} &= d_{yz} Y - d_{z2y} Z_2 + d_{z3y} Z_3 \\
 d_z F_{Ax} - d_x F_{Az} &= -d_{x12z} (X_1 + X_2) + d_{z1x} Z_1 - d_{z23x} (Z_2 + Z_3) \\
 d_x F_{Ay} - d_y F_{Ax} &= -d_{x1y} X_1 + d_{x2y} X_2 + d_{yx} Y
 \end{aligned} \tag{A.9}$$

The three moment equations in Eq.{A.9} can be written in the form  $Ax = b$  as shown in Eq.{A.10}. As stated the variables in matrix  $A$  can be calculated from Eq.{A.8} and all variables in vector  $b$  is known as they have been measured experimentally. The determinant of matrix  $A$  is calculated to be zero ( $\det(A) = 0$ ). This implies that matrix  $A$  is singular and it is not possible to invert it and we can therefore not solve for the application point coordinates  $d_x$ ,  $d_y$  and  $d_z$  using Eq.{A.10}. If, however, either  $d_x$ ,  $d_y$ , or  $d_z$  is known it is possible to calculate the other two variables using the set of equations in Eq.{A.9}.

$$\begin{bmatrix} 0 & F_{A_z} & -F_{A_y} \\ -F_{A_z} & 0 & F_{A_x} \\ F_{A_y} & -F_{A_x} & 0 \end{bmatrix} \begin{Bmatrix} d_x \\ d_y \\ d_z \end{Bmatrix} = \begin{Bmatrix} d_{y_z} Y - d_{z_2y} Z_2 + d_{z_3y} Z_3 \\ -d_{x_{12z}} (X_1 + X_2) + d_{z_{1x}} Z_1 - d_{z_{23x}} (Z_2 + Z_3) \\ -d_{x_{1y}} X_1 + d_{x_{2y}} X_2 + d_{y_x} Y \end{Bmatrix} \quad \{A.10\}$$

Considering the way the force is applied to the 6clc in the four load cases the following can be concluded. For Load case 1 and 2  $d_z$  is well defined whereas  $d_x$  and  $d_y$  is not as it may be anywhere within the envelope discussed in paragraph A.2.2.1. The same situation is present in Load case 4 where  $d_x$  is assumed to be well defined whereas  $d_y$  and  $d_z$  is not as they may be anywhere within the envelope created by the 32mm tube. For Load case 3 the application point is supposed to be well defined in  $d_x$ ,  $d_y$  and  $d_z$  as the actuator was attached to the 6clc via a spherical joint and yoke. This however may not guarantee that the practical application point coincides exactly with the theoretical point but it is assumed that the theoretical and practical application points for Load case 3 coincide.

When it is assumed that  $d_z$  is well defined for Load case 1 and Load case 2,  $d_y$  and  $d_x$  can be calculated using Eq.{A.9} from which the following equations are obtained for  $d_y$  and  $d_x$ :

$$d_y = \frac{d_{y_z} Y - d_{z_2y} Z_2 + d_{z_3y} Z_3 - d_z F_{A_y}}{F_{A_z}}$$

$$d_x = \frac{d_z F_{A_x} - (-d_{x_{12z}} (X_1 + X_2) + d_{z_{1x}} Z_1 - d_{z_{23x}} (Z_2 + Z_3))}{F_{A_z}}$$

$F_{A_z}$  is calculated from Eq.{A.8}. The remaining moment equation can be used as a check, as  $d_x$  and  $d_y$  substituted into Equation {A.11}, should be equal to zero:

$$d_x F_{A_y} - d_y F_{A_x} - (-d_{x_{1y}} X_1 + d_{x_{2y}} X_2 + d_{y_x} Y) = 0 \quad \{A.11\}$$

For Load case 4 it is assumed that  $d_x$  is well defined and  $d_y$  and  $d_z$  can be calculated using Eq.{A.9} from which the following equations are obtained for  $d_y$  and  $d_z$ :

$$d_y = \frac{d_x F_{A_y} - (-d_{x_{1y}} X_1 + d_{x_{2y}} X_2 + d_{y_x} Y)}{F_{A_x}}$$

$$d_z = \frac{-d_{x_{12z}} (X_1 + X_2) + d_{z_{1x}} Z_1 - d_{z_{23x}} (Z_2 + Z_3) + d_x F_{A_z}}{F_{A_x}}$$

$F_{A_x}$  is calculated from Eq.{A.8}. The remaining moment equation can be used as a check, as  $d_y$  and  $d_z$  substituted into Equation {A.12}, should be equal to zero:

$$d_y F_{A_z} - d_z F_{A_y} - (d_{y_z} Y - d_{z_2y} Z_2 + d_{z_3y} Z_3) = 0 \quad \{A.12\}$$

Table A.8 shows the application point calculated from the experimental measurements for Load cases 1, 2 and 4 calculated using the equations above. It also shows whether the adjustment falls within the envelope as well as the results from the test equations (Eq.{A.11} and Eq.{A.12}). The reader should note that the results of the test equations are given as a mean and a standard deviation because the application point may shift within the envelope as the force is applied and removed.

**Table A.8.** Application point

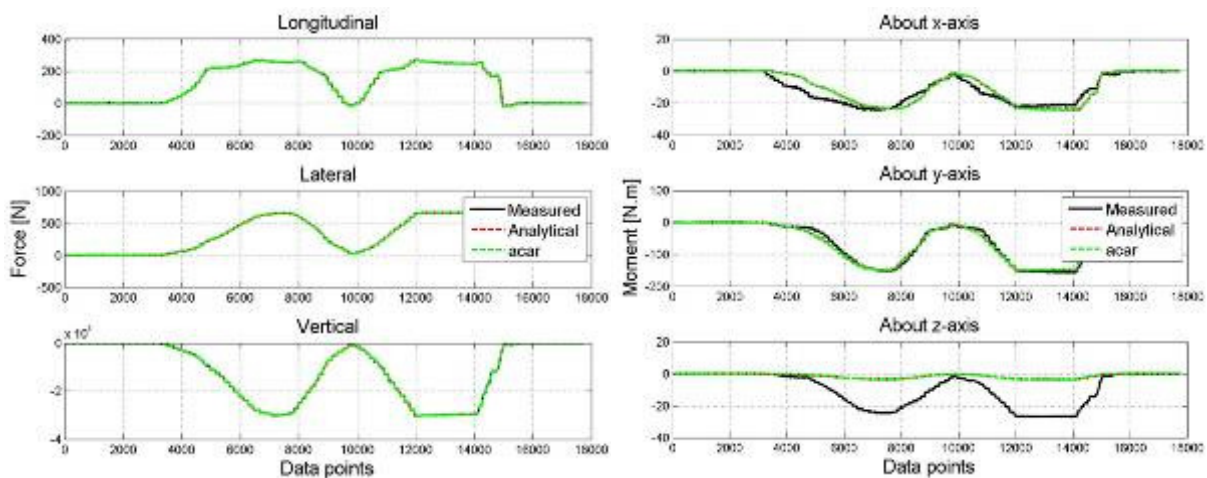
Load case	Application point: Theoretical	Application point: Calculated from measurements	Adjustment	Test equations	
				mean [N.m]	standard deviation [N.m]
1	[0, 0, <b>0.085</b> ]	[-0.0057,-0.00108, <b>0.085</b> ]	5.8mm < 16mm ⇒ within envelope	9.85	10.25
2	[0.0475, 0.04, <b>0.085</b> ]	[0.0421,0.0345, <b>0.085</b> ]	7.7mm < 16mm ⇒ within envelope	9.85	10.18
4	[ <b>0.0575</b> ,-0.0175, 0.101]	[ <b>0.0575</b> ,-0.0261,0.0955]	10.2mm < 16mm ⇒ within envelope	-83.6	67.5

Note: The coordinates shown in **orange** are the coordinates that are assumed to be known for the specific load case

From the results in Table A.8 it can be seen that the application point calculated from the experimental measurements falls within the envelope created by the 32mm tubing. The test equations are not satisfied with Load case 4 having the greatest deviation. This indicates that the application point that is calculated changes, within the envelope, as the force is applied. Although the test equation is not satisfied, the application point calculated from the experimental measurements will be used as they still fall within the envelope. The results for the two models, when using the experimentally calculated applied force orientation and application point, are shown next for all four load cases.

### Load case 1 and 2

From Figure A.32 and Figure A.33 it can be observed that there is an improvement in the correlation of the equivalent moments as well as in the forces in the uni-axial load cells when the experimentally calculated application is used in the models. However, the correlation of the forces in the uni-axial load cells  $X_1$  and  $X_2$  are still not good. This is true for both Load case 1 and 2 (see Figure A.33 and Figure A.35). Similarly, the correlation of the equivalent moment about the z-axis is also not good for both Load case 1 and 2 (see Figure A.32 and Figure A.34). Except for the correlation of the two uni-axial load cell forces  $X_1$  and  $X_2$  and the equivalent moment about the z-axis, good correlation is obtained for all the other equivalent forces and moments and forces in the uni-axial load cells.


**Figure A.32.** Comparison of equivalent forces and moments (Load case 1 – Experimental loading and application point)



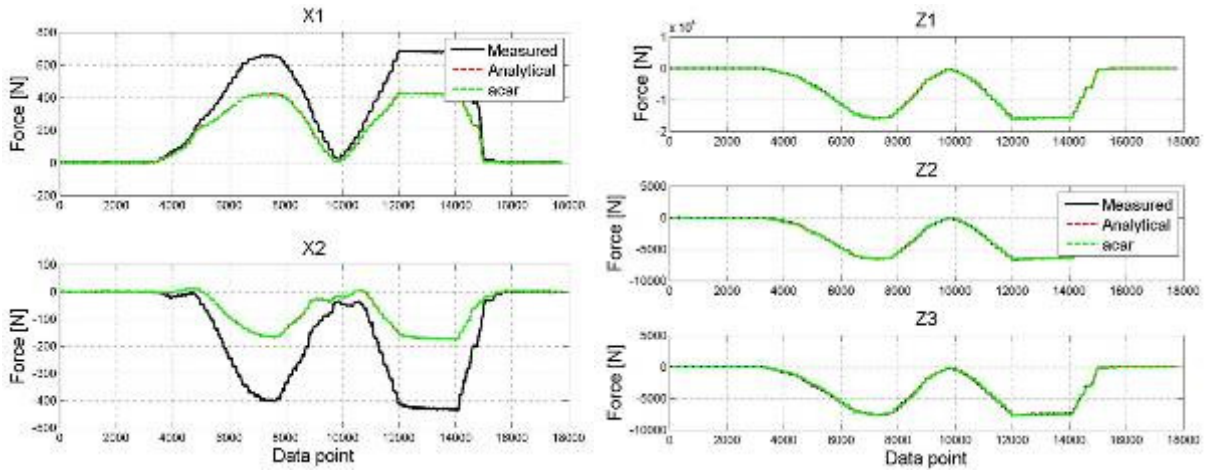


**Figure A.33.** Comparison of forces in uni-axial load cells orientated in the longitudinal and vertical direction (Load case 1 – Experimental loading and application point)

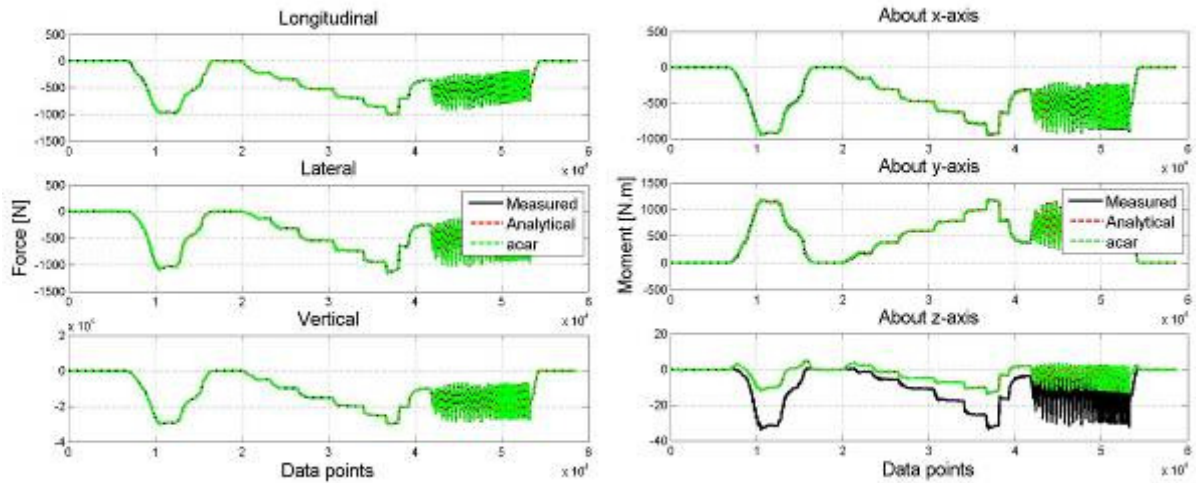


**Figure A.34.** Comparison of equivalent forces and moments (Load case 2 – Experimental loading and application point)

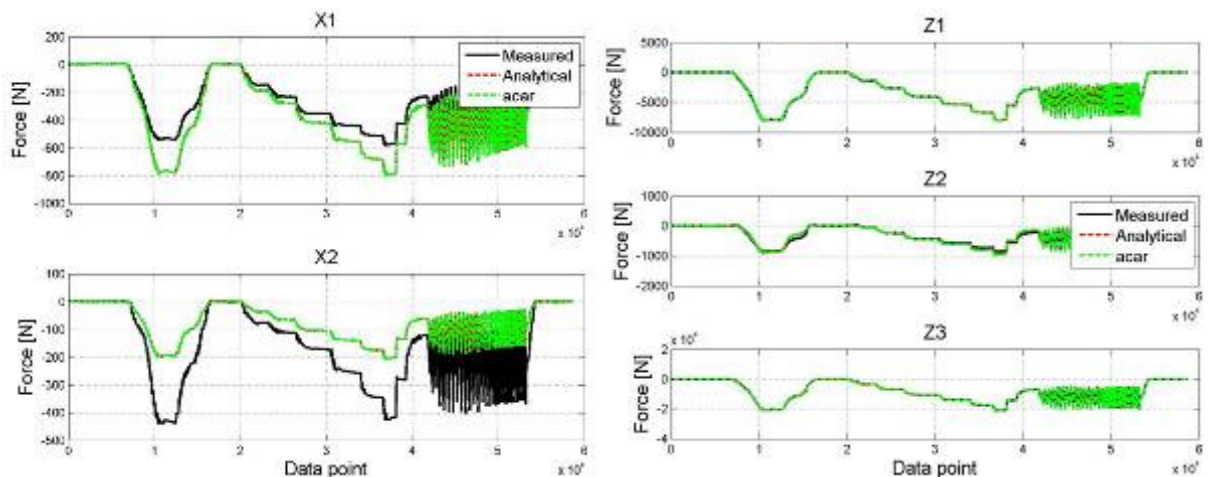
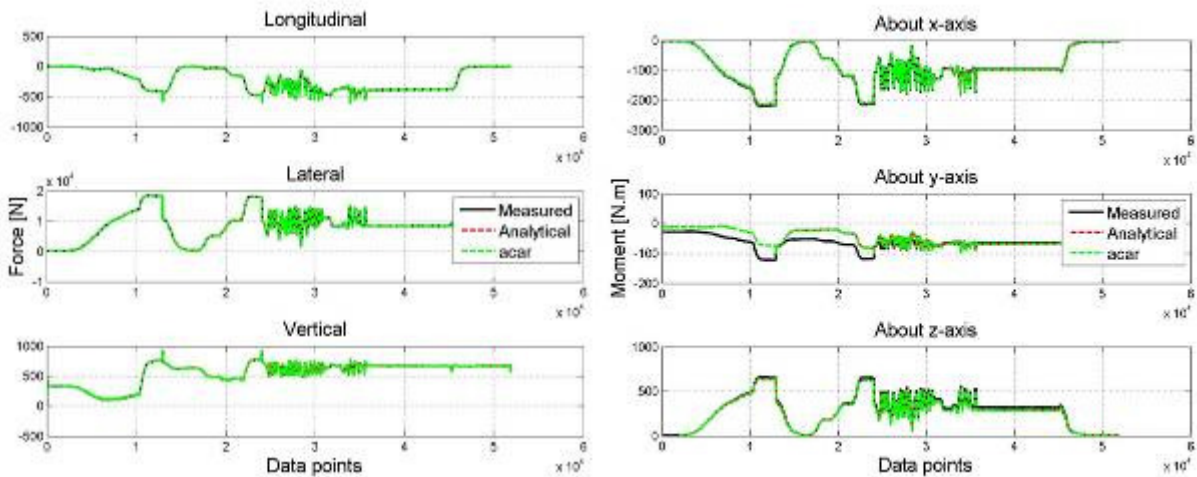


**Figure A.35.** Comparison of forces in uni-axial load cells orientated in the longitudinal and vertical direction (Load case 2 – Experimental loading and application point)

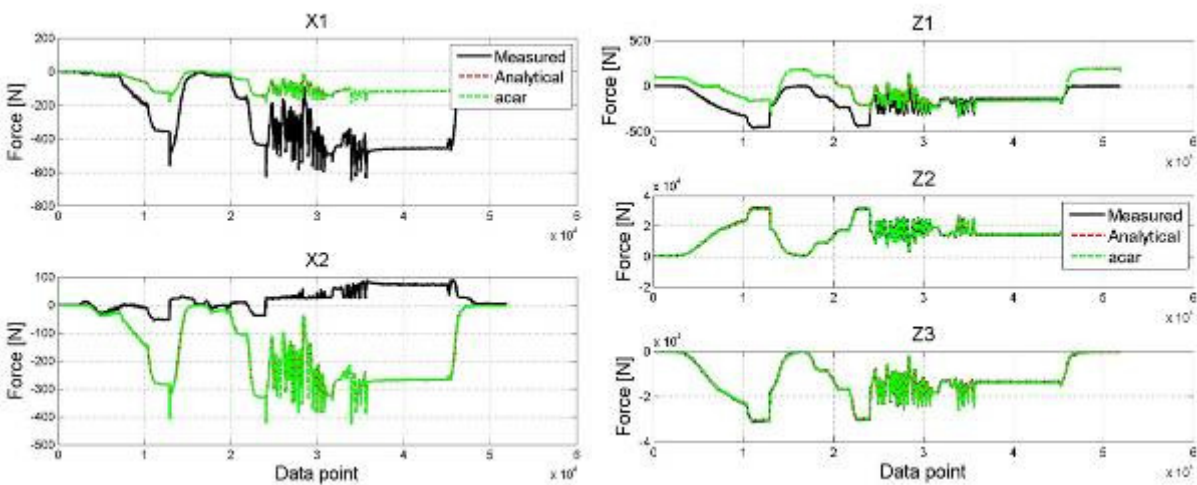
### Load case 3

Figure A.36 and Figure A.37 show the correlation between the models and the measured data when the experimentally calculated applied force orientation is applied to the two models.

The application point is not calculated from the experimental measurements as the loading was applied via a spherical joint and yoke. It was therefore assumed that the practical application point should be in close agreement with the theoretical application point. Therefore the theoretical application point is used for Load case 3. The equivalent forces results show good correlation. The forces in the uni-axial load cells  $X_1$ ,  $X_2$  and  $Z_1$  do not show good correlation which leads to the deviations in the correlation of the equivalent moment about the y-axis.



**Figure A.36.** Comparison of equivalent forces and moments (Load case 3 – Experimental loading and application point)



**Figure A.37.** Comparison of forces in uni-axial load cells orientated in the longitudinal and vertical direction (Load case 3 – Experimental loading and application point)

#### Load case 4

Figure A.38 and Figure A.39 show the correlation between the models and the measured data for Load case 4. The equivalent force results show good correlation. The forces in the uni-axial load cells  $Z_2$  and  $Z_3$  do not show good correlation which leads to the deviations in the correlation of the equivalent moment about the x-axis.

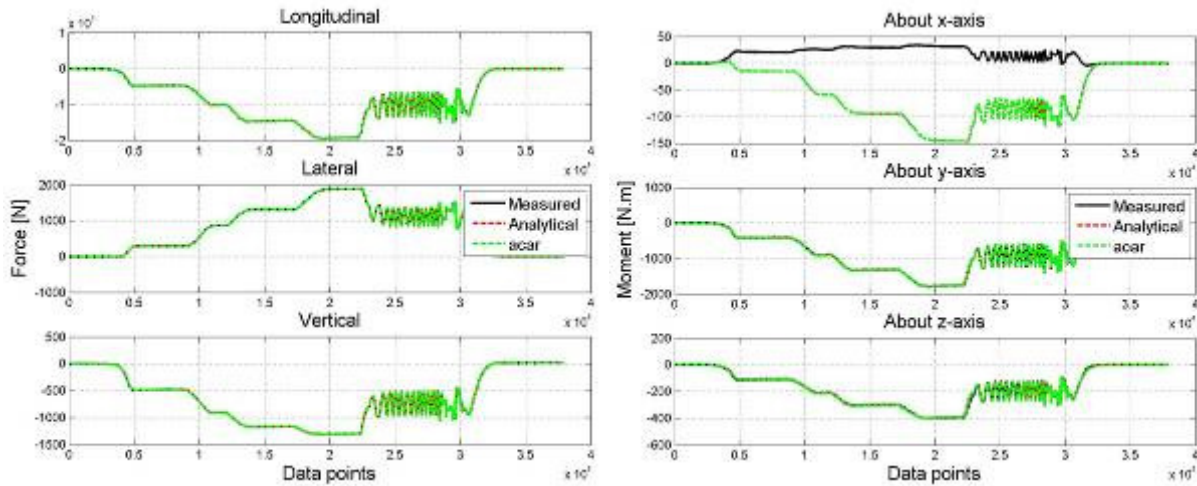


**Figure A.38.** Comparison of equivalent forces and moments (Load case 4 – Experimental loading and application point)

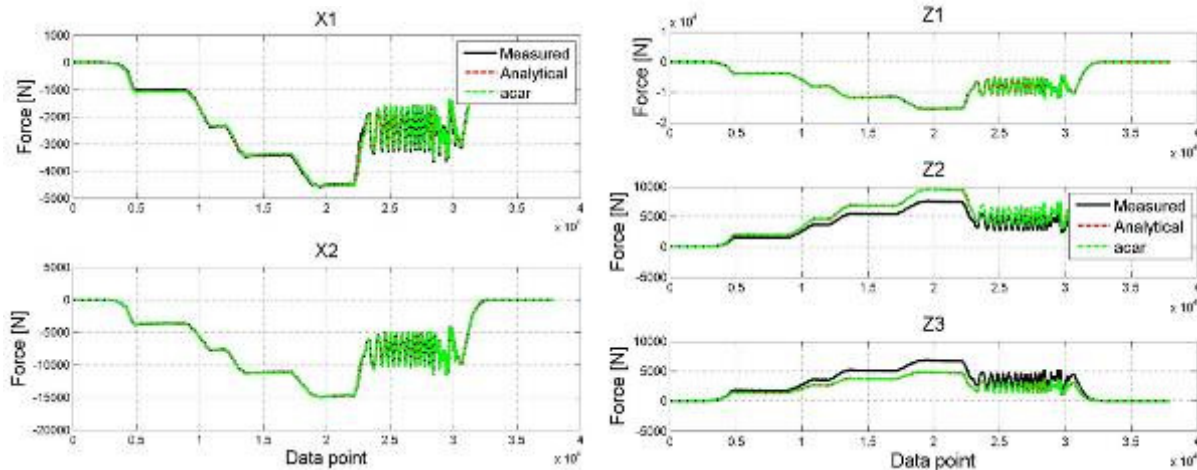


**Figure A.39.** Comparison of forces in uni-axial load cells orientated in the longitudinal and vertical direction (Load case 4 – Experimental loading and application point)

The force measurements from the two models were improved when the applied force and the application point, calculated from the experimental measurements, were used in the models. Good correlation is obtained between the physical 6clc and the two models' equivalent forces for all the load cases. The correlation for the equivalent moments are good but there are still some equivalent moments from the models that deviate from the experimental data. Possible causes for this may be due to the application point still not being exactly the same as the application point in the experimental setup.

#### A.2.4. Validation results for the rear 6clc

Paragraph A.2.2 and paragraph A.2.3 showed the validation results using the experimental measurements taken on the front 6clc. The two models will now be validated using the experimental measurements taken on the rear 6clc. Obtaining good results between the two models' "measurements", using the experimental measurements taken on the rear (physical) 6clc, and the experimental measurements will imply that the ADAMS/Car model can be used to model both the front and rear physical 6clcs.

The results for the four load cases (see Table A.4) are given in the following three paragraphs. The same ADAMS/Car model is used for the front and rear 6clc, the only difference is in the

practical application point that is used in the model. The experimentally calculated force orientation and application point are used in the two models. Table A.9 shows the application points used for the four load cases. For all the load cases, except for Load case 3, the experimentally calculated application point is used.

**Table A.9.** Application point (Rear 6clc)

Load case	Application point: Theoretical	Application point: Calculated from measurements	Adjustment	Test equations	
				mean [N.m]	standard deviation [N.m]
1	[0, 0, <b>0.085</b> ]	[-0.00465, 0.00327, <b>0.085</b> ]	5.7mm < 16mm ⇒ within envelope	-10.32	10.29
2	[0.0475, 0.04, <b>0.085</b> ]	[0.0472, 0.0356, <b>0.085</b> ]	4.4mm < 16mm ⇒ within envelope	-2.63	2.73
3	[0.035, -0.0175, 0.115]	N/A	N/A	N/A	N/A
4	[ <b>0.0575</b> , -0.0175, 0.101]	[ <b>0.0575</b> , -0.0133, 0.0951]	7.2mm < 16mm ⇒ within envelope	22.68	26.12

Note: The coordinates shown in **orange** are the coordinates that are assumed to be known in the specific load case

### Load case 1 and Load case 2

Figure A.40 and Figure A.41 show the results for Load case 1 and Figure A.42 and Figure A.43 show the results for Load case 2. The results for both load cases show that the correlation between the models' and the physical 6clc's measured forces in the uni-axial load cells  $X_1$  and  $X_2$  is not good. This causes the correlation of the equivalent moment about the z-axis also not to be good. This is similar to the results obtained in paragraph A.2.3.2.

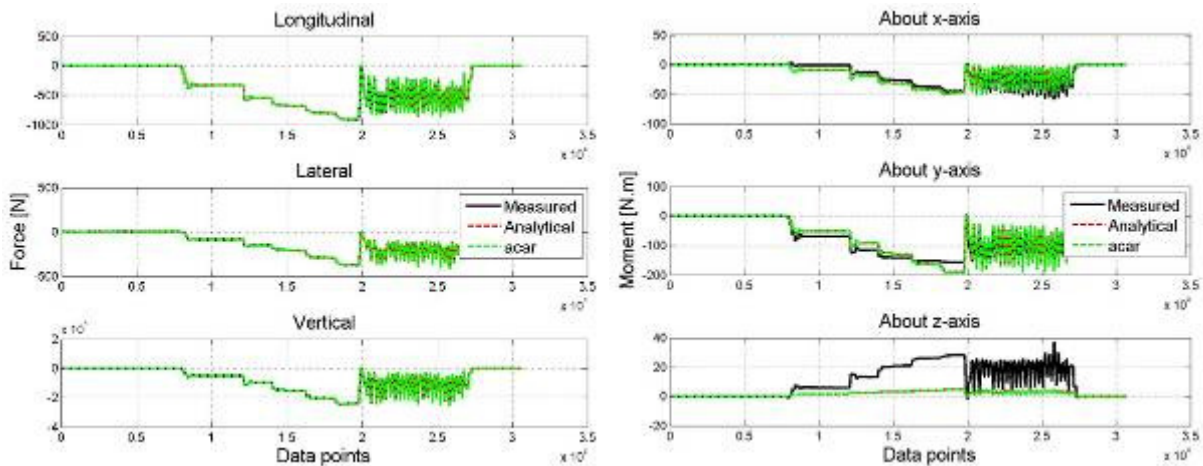


**Figure A.40.** Comparison of equivalent forces and moments (Load case 1 - Rear 6clc – Experimental loading and application point)

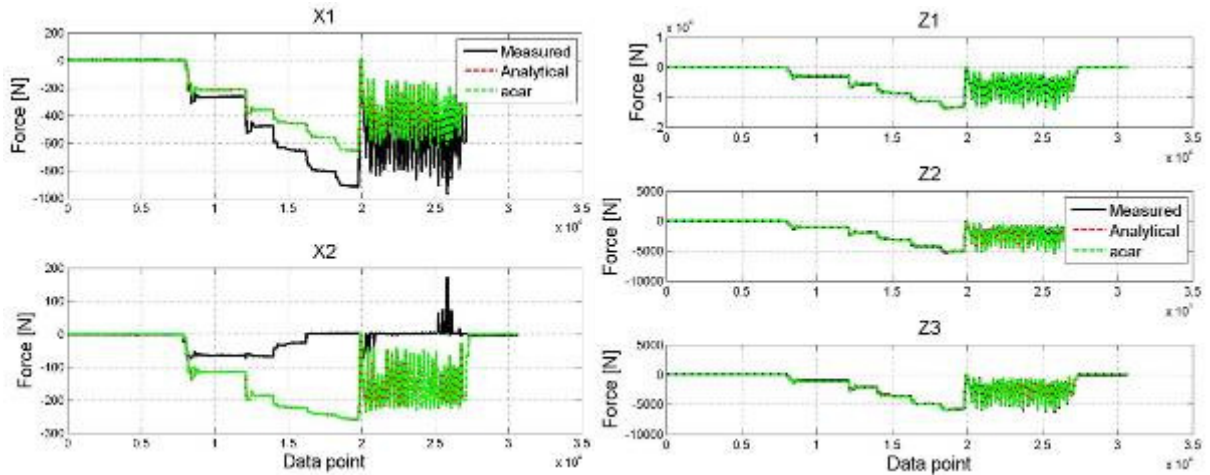


**Figure A.41.** Comparison of forces in uni-axial load cells orientated in the longitudinal and vertical direction (Load case 1 - Rear 6clc – Experimental loading and application point)

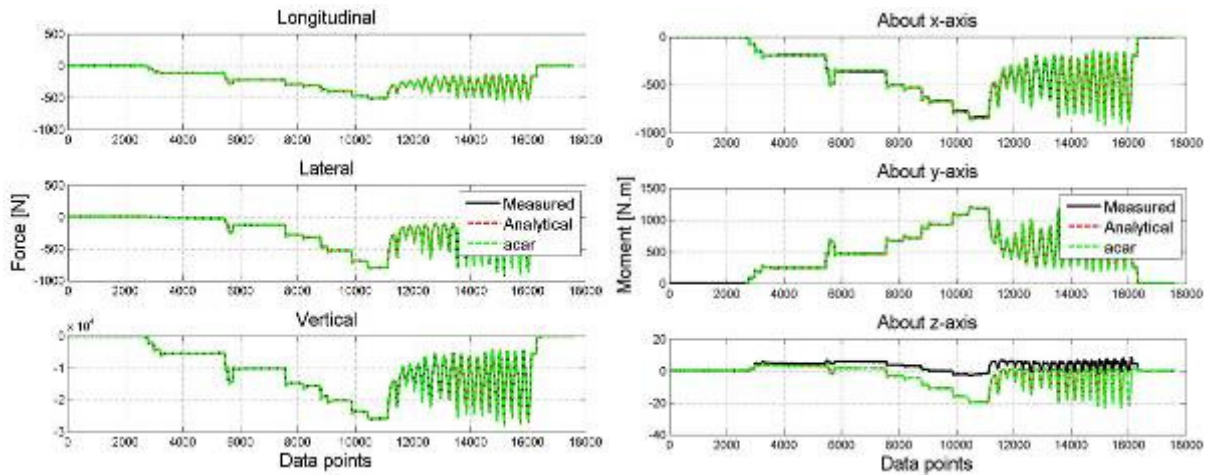


**Figure A.42.** Comparison of equivalent forces and moments (Load case 2 - Rear 6clc – Experimental loading and application point)

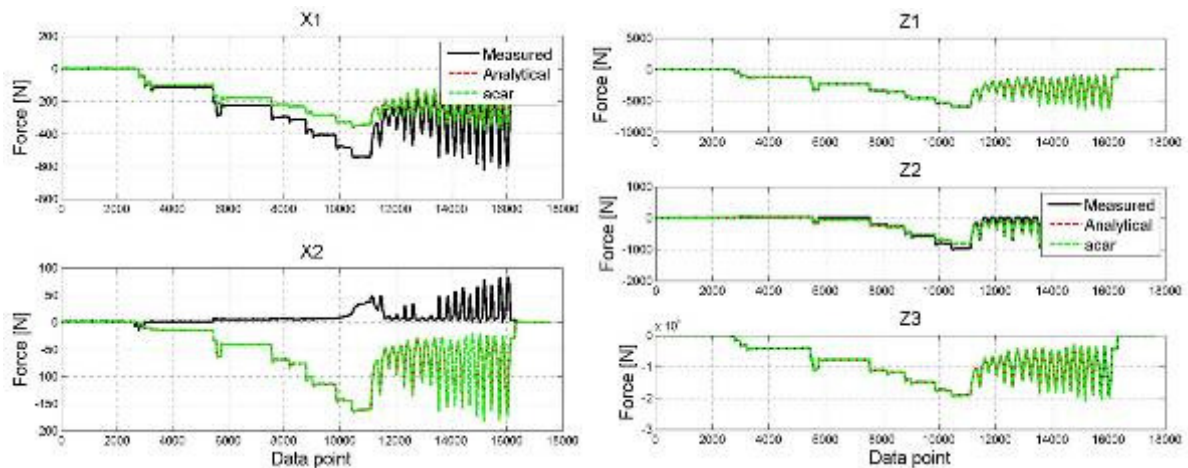


**Figure A.43.** Comparison of forces in uni-axial load cells orientated in the longitudinal and vertical direction (Load cell 2 - Rear 6clc – Experimental loading and application point)

### Load case 3

The correlation of the forces in the uni-axial load cells  $X_1$ ,  $X_2$  and  $Z_1$  is not as good as the correlation for the other uni-axial load cell forces (see Figure A.44). Except for the equivalent

moment about the y-axis, the other two equivalent moments and all three equivalent forces show good correlation (see Figure A.45).

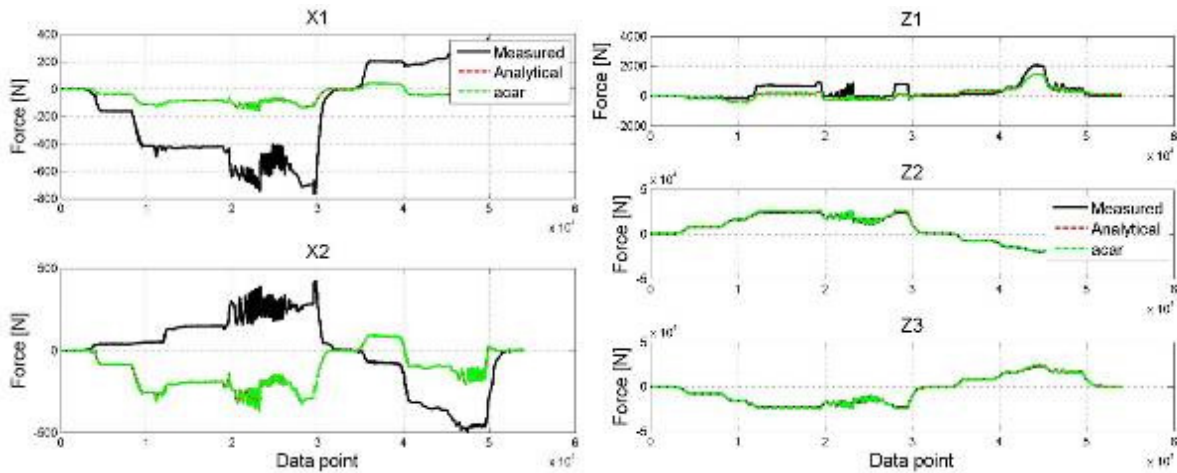


**Figure A.44.** Comparison of the forces in the uni-axial load cells orientated in the longitudinal and vertical direction (Load case 3 - Rear 6lc – Experimental loading and application point)

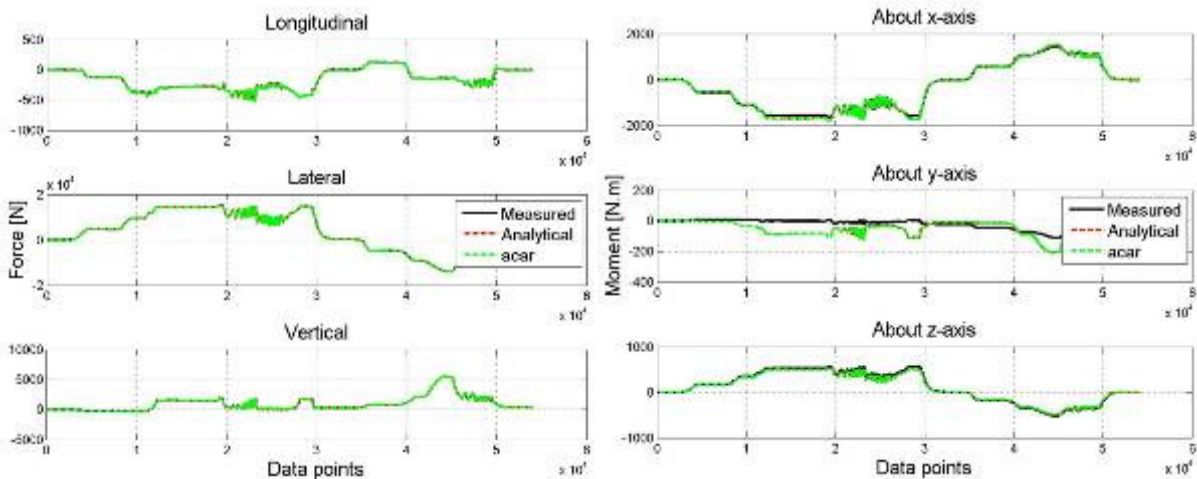


**Figure A.45.** Comparison of equivalent forces and moments (Load case 3 - Rear 6lc – Experimental loading and application point)

#### Load case 4

Figure A.46 and Figure A.47 show the results for Load case 4. Except for the forces in the uni-axial load cells  $Z_2$  and  $Z_3$  all the other uni-axial load cell forces show good correlation. The discrepancy between  $Z_2$  and  $Z_3$  causes the equivalent moment about the x-axis to deviate from the measured data. The other two equivalent moments and all three equivalent forces show good correlation.

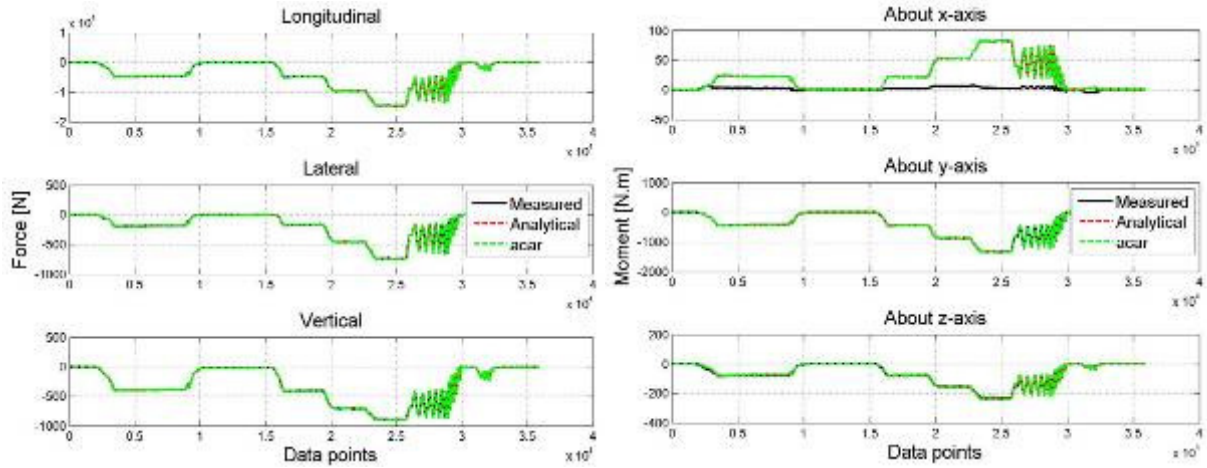


**Figure A.46.** Comparison of equivalent forces and moments (Load case 4 - Rear 6clc – Experimental loading and application point)

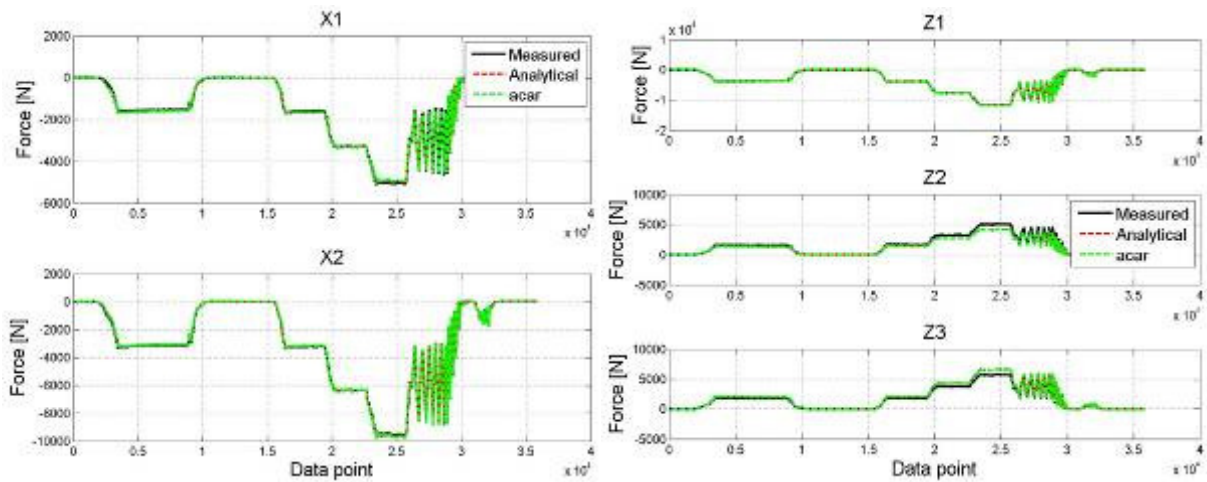


**Figure A.47.** Comparison of forces in uni-axial load cell orientated in the longitudinal and vertical direction (Load case 4 - Rear 6clc – Experimental loading and application point)

The validation results for the two models using the experimental measurements taken on the rear 6clc showed similar trends and correlation to that obtained when the measurements on the front (physical) 6clc were used.

### A.3. Conclusion

Twelve uni-axial load cells were calibrated and integrated into two six component load cells. The analytical equations for the 6clc were derived which calculates the equivalent forces and moments acting on the load cell. Using the analytical equations the feasibility of the 6clc concept was verified. An ADAMS/Car model was created to represent the 6clc and was also verified using the analytical equations. The analytical equations and the ADAMS/Car model were validated against experimental measurements. The results showed good correlation between the two models and the measured data when the experimentally calculated force orientation and application point were used in the two models. Good correlation was obtained for all the equivalent forces for all four load cases. The correlation of the equivalent moments tends to have one of the equivalent moments that do not have good correlation. This may be due to the application point between the physical 6clc and the model not being exactly the same.

From the verification and validation results it can be concluded that both the physical as well as the virtual 6clc can be used to measure the equivalent forces and moments. It is however suggested that a more rigorous validation process is undertaken which concentrates on having a experimental setup which enables better control over the orientation and application point of the applied force.



# Appendix B

## Theoretical stiffness of the multi-leaf spring

This appendix investigates the use of beam theory to calculate the two stiffness regimes observed on the force-displacement characteristic of the multi-leaf spring. The two stiffness regimes are associated with the solid beam and layered beam behaviour discussed in paragraph 2.2 of Chapter 3. The appendix will first present the equations that can be used to calculate the stiffness of the two regimes. The two stiffness regimes of the multi-leaf spring are calculated using two methods, 1) the principle of superposition from beam theory (Gere, 2004) and, 2) the equations in the SAE Spring Design Manual (1996).

### B.1. Calculating the theoretical stiffness

The stiffness of the two regimes of the multi-leaf spring is calculated by dividing the multi-leaf spring, shown in Figure B.1, into two cantilevers. It is assumed that the clamping in the clamped section is perfect meaning that this section acts like a solid beam without the possibility of slip between the individual blades. This result in the boundary condition shown in Figure B.1 and divides the leaf spring in a front and rear cantilever, The stiffness of the multi-leaf spring is calculated by first calculating the stiffness of the two cantilevers and then combining the cantilever stiffnesses to obtain the equivalent stiffness which represents the multi-leaf spring stiffness. As mentioned, two methods will be used to calculate the stiffness of the cantilever beams. The method of superposition, presented in paragraph B.1.1, is able to calculate the stiffness of both stiffness regimes whereas the second method using the equations in the SAE spring design manual (1996) is only able to calculate the stiffness of the regime associated with the layered beam behaviour.

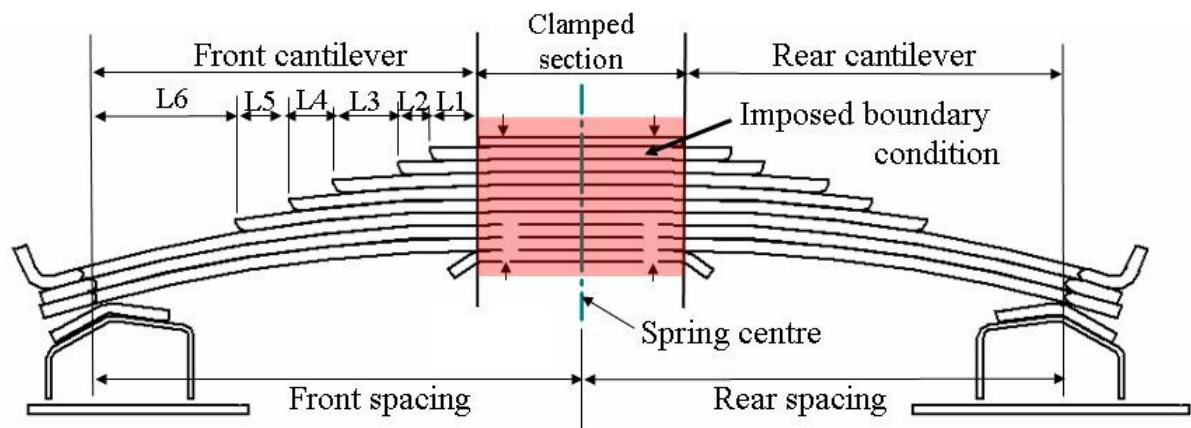


**Figure B.1.** Multi-leaf spring dimensions

Figure B.1 shows the dimensions for the multi-leaf spring. The lengths L1 to L5 represent the actual length and not the total length as the total length of each section is not in complete contact with the next blade. This is shown in Figure B.2.

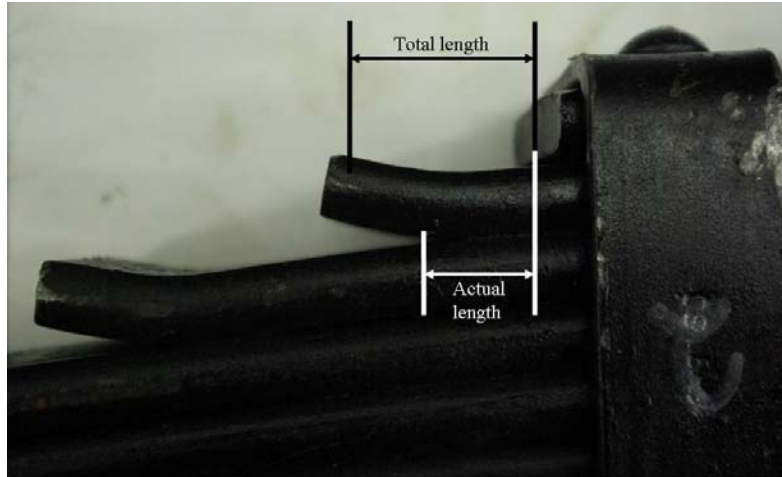


**Figure B.2.** Contact between blades at blade ends

### B.1.1. Principle of superposition

The theoretical stiffness of the spring's two stiffness regimes is calculated using the principle of superposition (Gere, 2004). The principle of superposition is used as the cantilever beam is non-prismatic. As mentioned the multi-leaf spring is divided into two cantilever beams (see Figure B.1), a front cantilever and rear cantilever. The stiffness of the cantilevers is calculated as follows. The cantilever is divided into prismatic sections (see Figure B.3). Calculating the deflection of each section and summing them gives the total deflection at G. Equation {B.1} shows the calculation of the deflection at G.

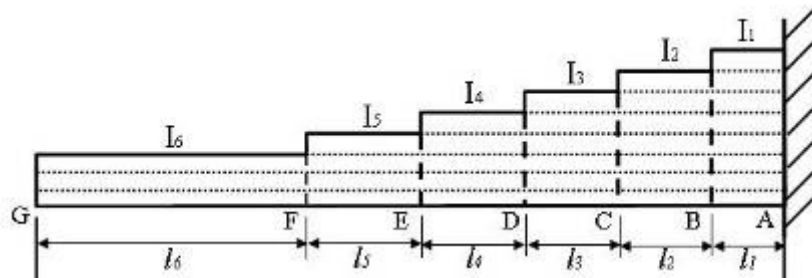


**Figure B.3.** Cantilever beam divided into sections with uniform cross section

$$\begin{aligned}
 \delta_G = & \delta_B + \theta_B l_2 + \delta_{C_2} + (\theta_B + \theta_C) l_3 + \delta_{D_2} + (\theta_B + \theta_C + \theta_D) l_4 + \delta_{E_2} \\
 & + (\theta_B + \theta_C + \theta_D + \theta_E) l_5 + \delta_{F_2} + (\theta_B + \theta_C + \theta_D + \theta_E + \theta_F) l_6 + \delta_{G_2}
 \end{aligned} \tag{B.1}$$

For  $\delta_B; \delta_{C_2}; \delta_{D_2}; \delta_{E_2}; \delta_{F_2}; \delta = \frac{PL^3}{3EI} + \frac{ML^2}{2EI}$  { Case 4 and Case 6 in Gere (2004)}

$$\delta_{G_2} = \frac{PL^3}{3EI} \tag{Case 4 in Gere (2004)}$$

For  $\theta_B; \theta_C; \theta_D; \theta_E; \theta_F; \theta = \frac{PL^2}{2EI} + \frac{ML}{EI}$  { Case 4 and Case 6 in Gere (2004)}

The deflections  $\delta_B, \delta_{C_2}, \delta_{D_2}, \delta_{E_2}$  and  $\delta_{F_2}$  are calculated using the equation given for  $\delta$  and with the correct values for  $P, L, M, E$  and  $I$  substituted into the equation for each section. Similarly, the angles of rotation  $\theta_B, \theta_C, \theta_D, \theta_E$  and  $\theta_F$  are calculated using the equation given for  $\theta$  and with the correct values for  $P, L, M, E$  and  $I$  substituted into the equation for each section. Substituting these equations into Equation {B.1}, and after some rearrangement, we obtain Equation {B.2} which is the stiffness ( $k$ ) of the non-prismatic cantilever. Note that in this equation the following shorthand notation is used:  $l_{62} = l_6 + l_5 + l_4 + l_3 + l_2$  etc.

$$k = \frac{P}{\delta_G} = E \left[ \frac{l_1^3}{3I_1} + \frac{l_2^3}{3I_2} + \frac{l_3^3}{3I_3} + \frac{l_4^3}{3I_4} + \frac{l_5^3}{3I_5} + \frac{l_6^3}{3I_6} + \frac{l_{62}l_{61}l_1}{I_1} + \frac{l_{63}l_{62}l_2}{I_2} + \frac{l_{64}l_{63}l_3}{I_3} + \frac{l_{65}l_{64}l_4}{I_4} + \frac{l_{66}l_{65}l_5}{I_5} \right]^{-1} \quad \text{{B.2}}$$

As discussed in paragraph 2.2 of Chapter 3 we expect the multi-leaf spring to have two stiffness regimes in its force-deflection characteristic. To calculate the stiffness of the two regimes the area moments of inertias ( $I_1$ - $I_6$ ) are calculated in one of two ways. For the instance were the beam is initially loaded or unloaded we assume that there is no slip between the blades (see paragraph 2.2 of Chapter 3). This causes the multi-leaf spring to act as a single non-prismatic beam (i.e. the spring is machined out of a solid billet and not made of stacked blades). For this instance the area moment of inertias are calculated as follows:

Multi-leaf spring considered as solid beam

$$I_i = \frac{bh_i^3}{12}$$

- with  $b$  = width of blade
- $h$  = thickness of individual blade
- $h_i$  =  $h$  x number of blades in section  $i$
- $i$  = section 1, 2, ..., 6

The other instance is when there is slip between the blades and the multi-leaf spring acts as a layered beam. In this case the blades are assumed to have no friction between them. The calculations of the area moments of inertias are as follows:

Multi-leaf spring considered as layered beam

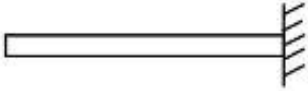
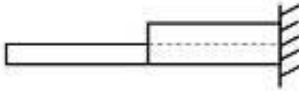
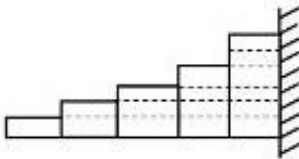
$$I_i = \frac{no l_i \times bh^3}{12}$$

- with  $b$  = width of blade
- $h$  = thickness of individual blade
- $i$  = section 1, 2, ..., 6
- $no l_i$  = number of blades in section  $i$

Equation {B.2} was derived for an eight blade multi-leaf spring with three full-length blades as indicated in Figure B.3. Table B.1 gives the general equations for the calculation of the theoretical spring stiffness of a leaf spring with a prismatic and non-prismatic cross-section. A leaf spring with a prismatic cross-section will for example consist of a single full length blade. A leaf spring with a non-prismatic cross-section will obviously consist of full length and non-full length blades.

Note that the stiffness Equation {B.2}, and the equations given in table B.1, assume that the initial rotation of the cantilever beam is zero.

**Table B.1.** Equation for calculating stiffness of prismatic and non-prismatic cantilever beams

Prismatic cantilever	
Number of sections, $n = 1$	
$k = E \left[ \frac{l^3}{3I} \right]^{-1}$	
Non-prismatic cantilevers	
Number of sections, $n = 2$	
$k = E \left[ \sum_{i=1}^n \frac{l_i^3}{3I_i} + \frac{l_n(l_n + l_{n-1})l_{n-1}}{I_{n-1}} \right]^{-1}$	
Number of sections, $n > 2$	
$k = E \left[ \sum_{i=1}^n \frac{l_i^3}{3I_i} + \sum_{i=1}^{n-2} \frac{l_i \sum_{j=i+1}^n l_j \sum_{k=1}^n l_k}{I_i} + \frac{l_n(l_n + l_{n-1})l_{n-1}}{I_{n-1}} \right]^{-1}$	

### B.1.2. SAE spring design manual

The SAE Spring Design Manual (1996) gives the following equation for the stiffness of a uniform strength cantilever beam:

$$k = \frac{2E \Sigma I}{l^3} .SF \tag{B.3}$$

- with
- $E$  - Young's modulus
  - $l$  - either for front cantilever ( $l_f$ ) or rear cantilever ( $l_r$ )
  - $SF$  - Stiffening factor. According to SAE Spring Design Manual (1996), for truck springs with untapered leaf ends and three full length blades  $SF = 1.25$
  - $\Sigma I$  - total moment of inertia

This equation can only be used to calculate the stiffness of the beam when it is considered to be behaving as a layered beam, in other words for the condition where the individual blades are able to move relative to one another.

### B.1.3. Calculating equivalent spring stiffness

In paragraph B.1.1 and B.1.2 we presented equations for the calculation of the stiffness of a cantilever beam. Seeing that the front and rear cantilever beam is in parallel the equivalent stiffness can be calculated by summing the stiffness of the front ( $k_a$ ) and rear ( $k_b$ ) cantilever beams:

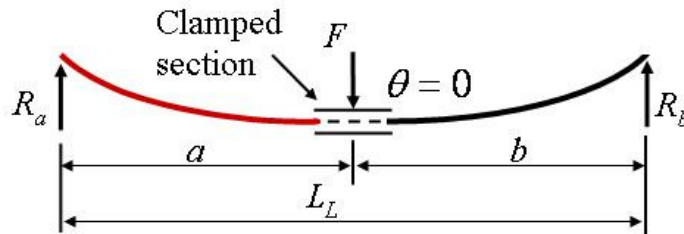
$$k_{eq} = k_a + k_b \quad \{B.4\}$$

The SAE spring design manual (1996) suggests using the following equation to combine the stiffnesses of the front and rear cantilevers:

$$k_{eq} = \frac{k_a k_b L^2}{k_a a^2 + k_b b^2} \quad \{B.5\}$$

The difference between Equation {B.4} and Eq.{B.5} will be shown by applying it to the two simple beams shown in Figure B.4. The figure shows two simply supported beams, one loaded symmetrically and the other one asymmetrically. Both beams are divided into a front and rear cantilever beam. In Figure B.4 the front cantilever is indicated in red and the rear cantilever in black. The clamped section is assumed to be infinitesimally small. The angle  $\theta$  represent the initial angle of rotation of the two cantilever beams. For a symmetric loading of the beam the initial angle of the cantilevers are zero, whereas for a asymmetric load case the initial angle of rotation of the two cantilever beams is non-zero.

Symmetric loading:  $a = b \Rightarrow \theta = 0$



Asymmetrical loading:  $a \neq b \Rightarrow \theta \neq 0$

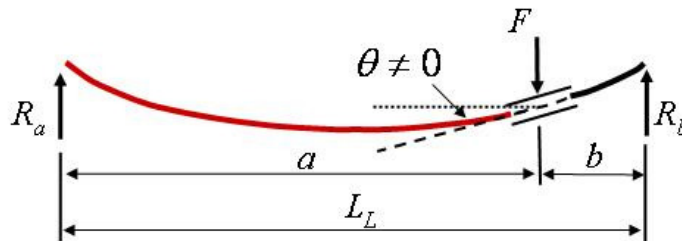


**Figure B.4.** Initial angle of rotation for symmetric and asymmetric loading

The stiffness of the two simple beams given in Figure B.4 will be calculated using the analytical equations for a simple beam. This will then be compared to the stiffness of the two beams that are calculated by dividing the simply supported beam into two cantilevers and then using Eq.{B.4} and Eq.{B.5}, respectively, to calculate the equivalent stiffness of the beam.

### B.1.3.1. Symmetrical loading

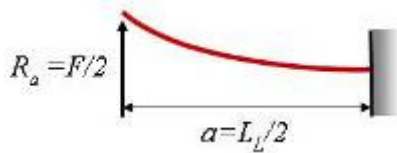
The stiffness of the symmetrically loaded simple beam can be calculated from Equation {B.6}. The equation for the deflection ( $\delta$ ) is at the point where the force is applied (Gere, 2004).

$$\delta = \frac{FL_L^3}{48EI}$$

$$k = \frac{48EI}{L_L^3} \quad [\text{N/m}] \quad \text{\{B.6\}}$$

The stiffness of the left and right cantilever beams are calculated using the equation given in Table B.1 for the prismatic cantilever beam. The calculation of the stiffness of the front and rear cantilever beams is given below:

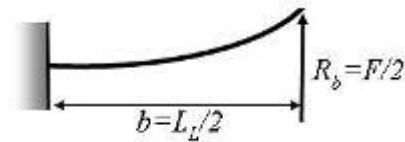
Left cantilever



The stiffness is calculated using the formulae for the prismatic beam given in Table B.1:

$$k_a = \frac{24EI}{L_L^3}$$

Right cantilever



The stiffness is calculated using the formulae for the prismatic beam given in Table B.1:

$$k_b = \frac{24EI}{L_L^3}$$

Using Eq.{B.4} to combine the stiffness of the two cantilevers we obtain the following equivalent stiffness:

$$\begin{aligned} k_{eq} &= k_a + k_b \\ &= \frac{24EI}{L_L^3} + \frac{24EI}{L_L^3} \\ &= \frac{48EI}{L_L^3} \end{aligned}$$

Using Eq.{B.5} to obtain the equivalent stiffness we get:

$$\begin{aligned} k &= \frac{k_a k_b L^2}{k_a a^2 + k_b b^2} \\ &= \frac{48EI}{L^3} \end{aligned}$$

Using either Eq.{B.4} or Eq.{B.5} we obtain the same stiffness as was calculated by the analytical equation for the stiffness of the simply supported beam with symmetric loading. The next paragraph will look at the same calculations but now applied to a simply supported beam with asymmetric loading.

### B.1.3.2. Asymmetrical loading

The stiffness of the asymmetrically loaded beam (shown in Figure B.4) can be calculated from Equation {B.7}. The equation for the deflection ( $v$ ) is at the point where the force is applied (Gere, 2004). It is assumed that  $a \geq b$ .

$$v = \frac{Pba}{6L_L EI} (L_L^2 - b^2 - a^2) \quad \{B.7\}$$

$$k = \frac{6L_L EI}{ba(L_L^2 - b^2 - a^2)} \quad \{B.8\}$$

Before the stiffness of the front and rear cantilever beams is calculated, the reaction forces ( $R_a$  and  $R_b$ ) of the simply supported beam are calculated. The following two equations are obtained by summing all the forces in the vertical direction and summing the moments about the point where the force  $F$  is applied.

$$\begin{aligned} \sum F_z = 0: R_a + R_b &= F \\ \sum M_c = 0: aR_a - bR_b &= 0 \end{aligned}$$

Solving these two equations simultaneously by multiplying the force equation with  $a$  and subtracting the moment equation from the new force equation we obtain:

$$R_b = \frac{aF}{L_L}$$

Substituting  $R_b$  into the original force equation we obtain:

$$R_a = \frac{bF}{L_L}$$

Now that the two reaction forces ( $R_a$  and  $R_b$ ) are known, the simple beam will be divided into two cantilever beams and their stiffnesses calculated. As was shown in Figure B.4 the point where the force  $F$  is applied will serve as the point for dividing the simple beam into two cantilevers. In calculating the stiffness of the two cantilever beams the slope of the beam at the force application point is required to calculate the correct deflection of each cantilever and infer the stiffness. Figure B.5 shows the calculation of the deflection at the end points of the simply supported beam (which are also the ends of the two cantilever beams) by using superposition. Figure B.5 shows that the deflection of the simply supported beam can be calculated by assuming that the two cantilevers have a zero initial angle of rotation. The deflection of the two cantilevers is calculated with the deflection, due to the angle of rotation of the undeformed cantilevers, added to obtain the deflection of the simply supported beam.

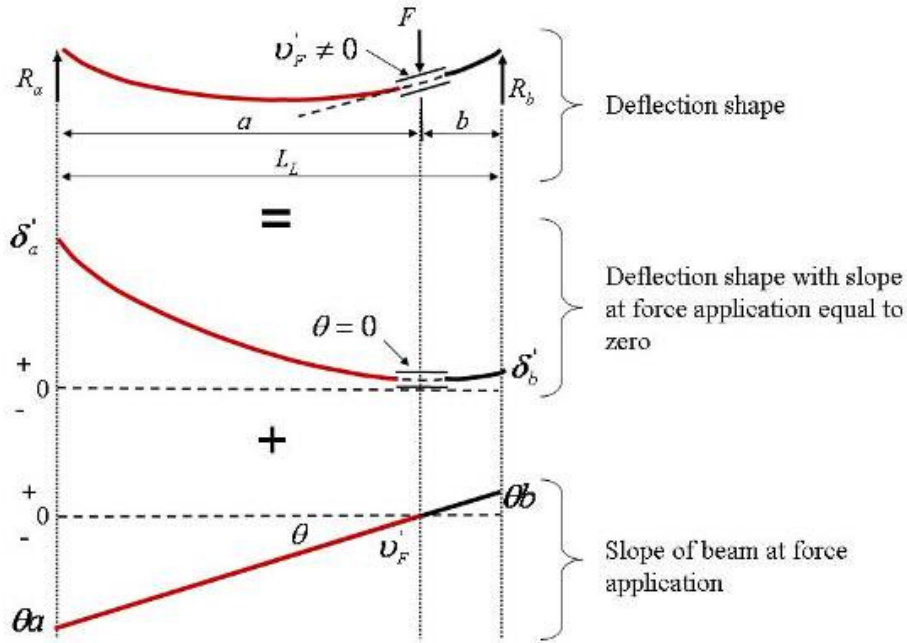
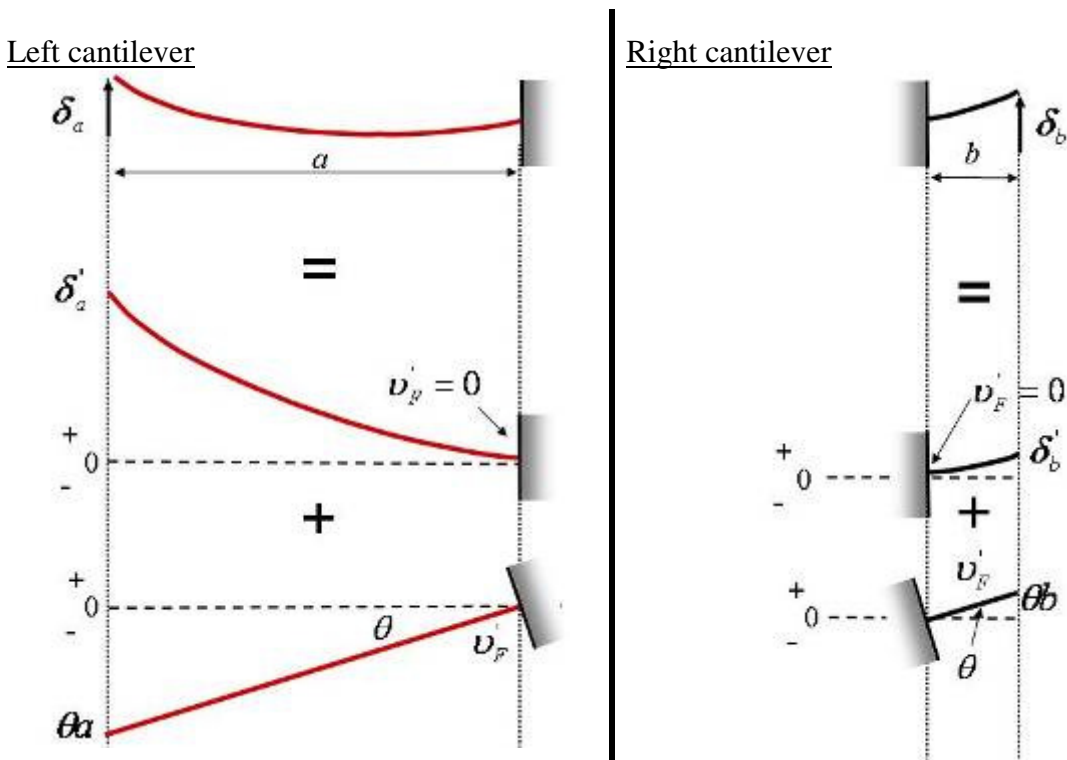


**Figure B.5.** Decomposition of deflection of simple beam

The deflection of the cantilevers, with the initial angle of rotation set to zero, is calculated with the deflection equation for a cantilever beam which was used to obtain the stiffness of the cantilever beam in Eq.{B.6}. The slope at the point of force application of the simple beam can be calculated with the following equation (Gere, 2004):

$$v'_F = -\frac{Fb}{6L_L EI} (L_L^2 - b^2 - 3a^2)$$

From this equation the angle of rotation can be calculated as  $\theta = \tan^{-1} v'_F$ . The stiffness of the two cantilevers using the method mentioned in Figure B.5 is shown below.





Deflection:

$$\begin{aligned}\delta_a &= \delta'_a - a\theta \\ &= \frac{R_a a^3}{3EI} - a\theta \\ &= \frac{bFa^3}{3EIL_L} - a\theta\end{aligned}$$

Stiffness:

$$\begin{aligned}k_a &= \frac{R_a}{\delta_a} \\ &= \frac{bF}{\frac{bFa^3}{3EI} - a\theta L_L}\end{aligned}$$

Deflection:

$$\begin{aligned}\delta_b &= \delta'_b + b\theta \\ &= \frac{R_b b^3}{3EI} + b\theta \\ &= \frac{aFb^3}{3EIL_L} + b\theta\end{aligned}$$

Stiffness:

$$\begin{aligned}k_b &= \frac{R_b}{\delta_b} \\ &= \frac{aF}{\frac{aFb^3}{3EI} + b\theta L_L}\end{aligned}$$

The stiffness of the front and rear cantilever beam calculated above can now be used in either Eq.{B.4} and Eq.{B.5} to calculate the equivalent beam stiffness. This equivalent beam stiffness can then be compared to the stiffness calculated from the Eq.{B.8}. In order to evaluate and compare the results from Eq.{B.4}, Eq.{B.5} and Eq.{B.8}, the following values for the parameters in these equations are used:

$$\begin{aligned}a &= 0.7\text{m} \\ b &= 0.3\text{m} \\ L_L &= 1\text{m} \\ F &= 1000\text{N} \\ E &= 207 \times 10^9 \text{Pa} \\ I &= 1.7 \times 10^{-8} \text{m}^4\end{aligned}$$

Table B.2 shows the results obtained from Eq.{B.4}, Eq.{B.5} and Eq.{B.8}. From these results it can be seen that the deflection calculated from the two cantilevers are equal to the deflection calculated from the simple beam Equation {B.7}. Similarly, the stiffness calculated using Equation {B.4} and Eq.{B.5} give the same answer as was calculated for the simple beam from Equation {B.8}.

**Table B.2.** Results from two cantilevers compared with results from simply supported beam

	Deflection [m]	Stiffness [kN/m]
Simple beam	0.004177	Using Eq.{B.8}
		239.4
Two cantilever beams	0.004177 ( $\delta_a = \delta_b$ )	Using Eq.{B.4}
		239.4
		Using Eq.{B.5}
		239.4

### B.1.3.3. Conclusion

From the results obtained for the symmetric and asymmetric loaded simply supported beam it seems that the method of dividing the simply supported beam into two cantilevers, calculating their stiffness and then combining it with either Eq.{B.4} and Eq.{B.5} gives the same results as that calculated from the stiffness equation for the simply supported beam. However, it was

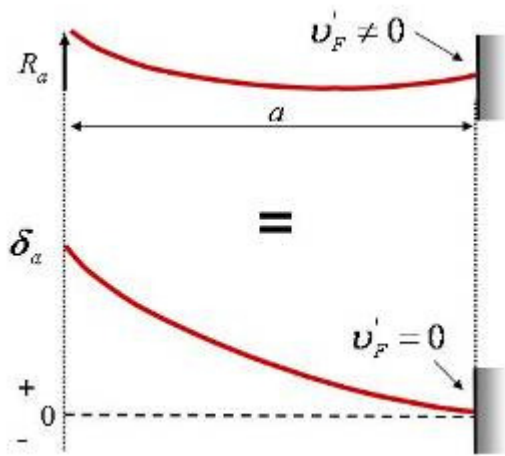
assumed at the beginning of the analysis that the clamped length is infinitesimally small. When the clamped length becomes longer the calculation of the slope of the beam may become increasingly more inaccurate as it deviates from the analytical deflection shapes of the simply supported beam. Therefore, it may become difficult to calculate the initial angle of rotation of the cantilever beams accurately. Not being able to include the initial angle of rotation in the calculation of the stiffness of the two cantilevers will lead to errors in the stiffness calculated. The following paragraph investigates the effect of the initial angle on the results of the stiffness calculations and how with the use of Eq.{B.5} this problem is circumvented.

### B.1.3.4. Neglecting the initial angle of the cantilevers

With a longer clamp section the analytical equation for calculating the slope of the simply supported beam may become inaccurate. This implies that it may become difficult to calculate the initial angle of rotation of the cantilever beams and therefore make it difficult to calculate the stiffness accurately. The equations for calculating the stiffness of the two cantilevers, without including the initial angle of rotation, are given in Table B.3. The calculation of the deflection only includes the deflection due to the deformed cantilever with an initial angle of rotation set to zero. It neglects the second part of the deflection, the deflection due to the initial angle of rotation of the cantilever, which was discussion in Figure B.5.

**Table B.3.** Equations for calculating stiffness of cantilevers (Neglecting initial angle of rotation)

#### Left cantilever



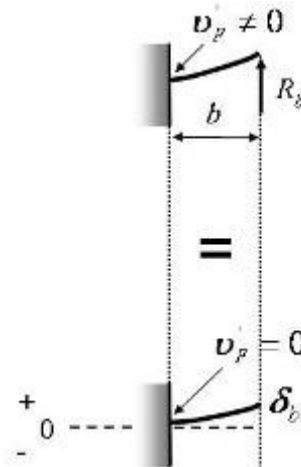
Deflection:

$$\delta_a = \frac{R_a a^3}{3EI} = \frac{bFa^3}{3EIL_c}$$

Stiffness:

$$k_a = \frac{R_a}{\delta_a} = \frac{3EI}{a^3}$$

#### Right cantilever



Deflection:

$$\delta_b = \frac{R_b b^3}{3EI} = \frac{aFb^3}{3EIL_c}$$

Stiffness:

$$k_b = \frac{R_b}{\delta_b} = \frac{3EI}{b^3}$$

From the equation given in Table B.3 it is clear that the deflection calculated for the two cantilevers will not be equal. The two cantilevers that are used to represent the simply supported beam are in parallel and should therefore experience the same deflection. Therefore from the results of the deflections it is clear that the exclusion of the initial angle of rotation of

the cantilever beams causes the incorrect calculation of the deflection. It is reasonable to expect that when the equivalent stiffness is calculated with either Eq.{B.4} and Eq.{B.5} that the incorrect simply supported beam stiffness will be obtained. Again Eq.{B.4}, Eq.{B.5} and Eq.{B.8} are evaluated and compared but with Eq.{B.4} and Eq.{B.5} using the front and rear cantilever stiffness calculated with the initial angle of rotation neglected. The equations are evaluated using the same values for the parameters as was used in paragraph B.1.3.2. The results are given in Table B.4.

**Table B.4.** Results from two cantilevers (initial angle of rotation neglected) compared with results from simply supported beam

	Deflection [m]	Stiffness [kN/m]
Simple beam	0.004177	Using Eq.{B.8}
		239.4
Two cantilever beams	$\delta_a = 0.009747$	Using Eq.{B.4}
		421.8
	$\delta_b = 0.00179$	Using Eq.{B.5}
		239.4

As expected the deflection of the two cantilevers differs, however, even though the deflection of the two cantilever beams is incorrect, the correct stiffness is obtained for the simple beam when using Eq.{B.5} to calculate the equivalent stiffness.

### B.1.4. Validation of theoretical stiffness calculation

In paragraph B.1.1 and B.1.2 equations for the calculation of the stiffness of a cantilever beam were presented. It was shown that the stiffness of a simply supported beam can be calculated by dividing the beam into two cantilever beams, calculating their stiffness and using Eq.{B.5} to calculate the equivalent stiffness. This method was shown to work for a symmetrically loaded as well as asymmetrically loaded simply supported beam. This method, with the use of Eq.{B.5}, does not require that the initial angles of rotations of the two cantilever beams be included. This makes the method useful when considering multi-leaf spring which have large clamped section and therefore may cause difficulties in calculating the slope of the multi-leaf spring accurately with analytical equations. The main reason for not being able to accurately calculate the slope of the multi-leaf spring is that for certain configurations of the leaf spring (especially concerning the clamped section length) it deviates from the simply supported beam's deflection shape which is used to approximate the multi-leaf spring.

The method will now be used to calculate the stiffnesses of the two regimes observed in the force-displacement characteristics of the multi-leaf spring considered in this study. The method of superposition and the SAE spring design manual (1996) is used to calculate the stiffness of the regime associated with the layered beam behaviour. The stiffness of the regime associated with the solid beam behaviour is calculated only with the method of superposition. In order to calculate the theoretical stiffness of the multi-leaf spring, the leaf spring is divided into two cantilever beams as was shown in Figure B.1. The stiffness of the two cantilevers are calculated, for both the layered and solid beam states, and combined into the multi-leaf spring stiffness for the layered and solid beam states using Eq.{B.5}.

Figure B.6 shows the correlation between the theoretically calculated stiffness and the experimentally measured force-displacement characteristic of the multi-leaf spring. Note that

the theoretical calculated stiffnesses shown in Figure B.6 are significantly higher than the stiffnesses observed in the experimental force-displacement characteristic.

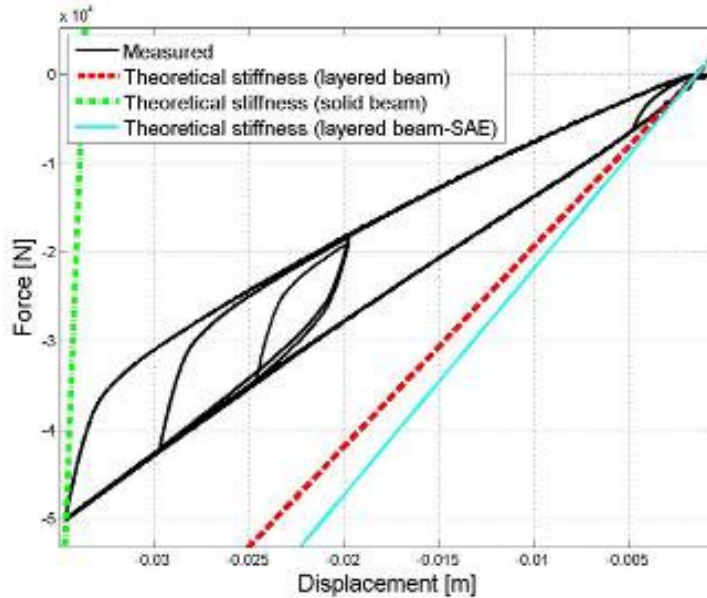


**Figure B.6.** Theoretical calculation of the two stiffness regimes

The deviation between the stiffness shown on the experimental and theoretically calculated force-displacement characteristics in Figure B.6 is large for both regimes. A possible cause for this might be from the assumption made in regards to the clamping in the clamped section. At the beginning of the Appendix it was assumed that the clamping in the clamped section is such that the individual blades within the clamped section are not able to move relative to one another implying that for this section the blades acted as a solid beam. This resulted in the system with the boundary conditions as was shown in Figure B.1. The imposed boundary conditions will definitely have an effect on the stiffness calculated for the leaf spring. The boundary condition effectively governs the effective length (or loaded length) of the leaf spring. As was shown in Chapter 2 the stiffness of a leaf spring is very sensitive to the loaded length. It was also shown in Chapter 2 that the stiffness of the leaf spring is sensitive to the preload of the U-bolts that are used to attach the axle to the leaf spring. The U-bolts are the components that apply the clamping force experienced in the clamped section. The sensitivity that was seen in the stiffness when changing the U-bolt preload was due to the boundary condition being changed. It is therefore expected that the theoretical stiffness will be just as sensitive to the boundary conditions of the clamped section as it will influence the loaded length used in the theoretical calculations. The effect of the clamping assumption and the resulting boundary condition on the theoretical stiffness calculation is investigated in more detail in the following paragraph.

## B.2. Effect of the clamping assumption on the theoretical stiffness

It was mentioned that the assumption made with respect to the clamped section will influence the loaded length of the leaf spring and therefore affect the stiffness. Considering the equation for the stiffness of a prismatic cantilever beam given as Eq. {B.9} we can see that the stiffness

has a relation of  $k \propto h^3$  and  $k \propto \frac{1}{L^3}$ .

$$k = \frac{Ebh^3}{4L^3} \quad \{B.9\}$$

From Eq.{B.9} it is clear that the stiffness has a high sensitivity to the thickness of the beam ( $h$ ) and the length of the beam ( $L$ ). Therefore, before we investigate the effect of the clamping assumption further we will confirm that the thickness used in the theoretical calculations is indeed the same as the thickness of the blades in the physical leaf spring. The thickness of each blade was measured at seven points spaced over the length of the blade. Table B.5 shows the measurements for the different blades and it can be seen that the thickness is rather uniform over the length of the blade; therefore the deviation in the theoretical stiffness observed in Figure B.6 is most probably not due to an incorrect thickness used in the theoretical stiffness calculations.

**Table B.5.** Blade thickness measurements

Measurements	1	2	3	4	5	6	7	Average	Std
<b>Blade 8</b>	14.1	14.1	14.1	14.1	14.1			14.1	0
<b>Blade 7</b>	14.05	14.1	14.05	14.05	14.1			14.07	0.0274
<b>Blade 6</b>	14	14	14	14.05	14.1			14.03	0.0447
<b>Blade 5</b>	14.15	14	14	14.05	14			14.04	0.0652
<b>Blade 4</b>	14	14	14	14.1	14.1			14.04	0.0548
<b>Blade 3</b>	14	14	14	13.95	13.95	13.8	13.8	13.93	0.09
<b>Blade 2</b>	13.8	13.9	14	13.95	14.05	14	13.9	13.94	0.084
<b>Blade 1</b>	14.1	14.05	14.1	13.95	14.05	13.9	13.9	14	0.089

The effect of the loaded length of the leaf spring on the stiffness is now investigated. The loaded length is a result of the assumption that is made for the type of clamping that is present in the clamped section. Considering the front cantilever the loaded length corresponds to the length of the cantilever (see Figure B.7). Figure B.7 shows the difference between the loaded length when the clamping in the clamped section is considered to be ideal and when there is no clamping. Up to now it has been assumed that the clamping is ideal. From Figure B.7 and Eq.{B.9} it is easy to deduct that the stiffness of the front cantilever using the assumption of ideal clamping will be higher than the stiffness of the cantilever for which no clamping is assumed.

The comparison in Figure B.6 showed that the theoretical stiffness, when ideal clamping is assumed, is higher than the stiffness observed on the experimental force-displacement characteristic. Therefore, when we assume that there is no clamping, the theoretical stiffness should be lower. The result of the theoretical stiffness, with the assumption of no clamping, is shown in Figure B.8. From this figure it can be seen that the theoretical stiffness is indeed lower and that it correlates well with the stiffness observed on the experimental force-displacement characteristic.

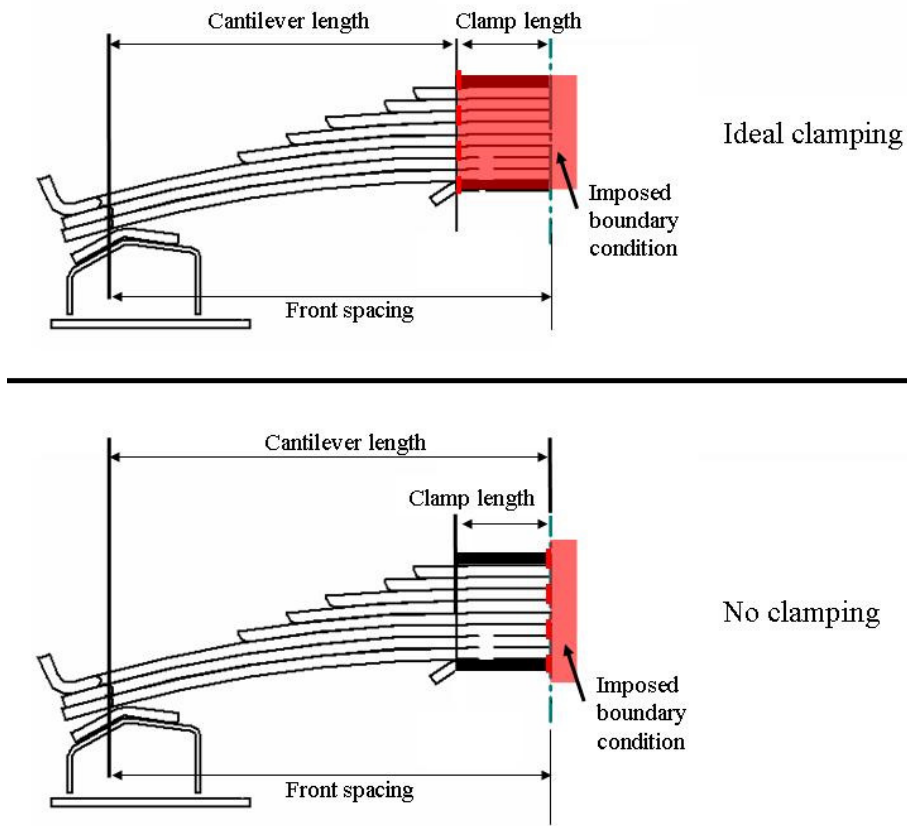


Figure B.7. Ideal vs. no clamping

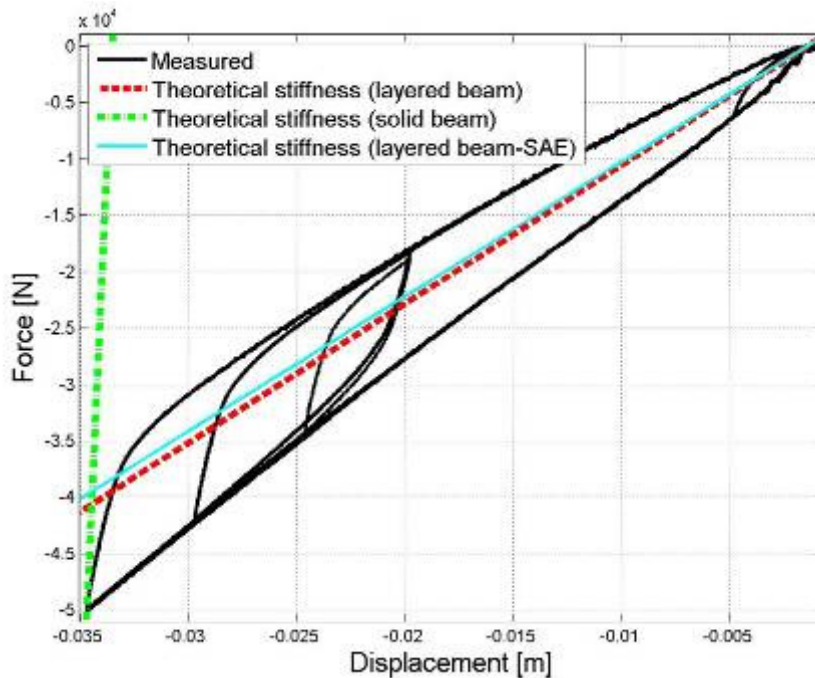


Figure B.8. Comparison between the measured force-displacement characteristic and the theoretically calculated stiffness assuming no clamping i.e. theoretical clamp length = 0m.

The theoretical stiffness of the two regimes was calculated using either the assumption of ideal clamping or no clamping. It should however be noted that the clamping may be between the ideal and no clamping assumption. The results from Figure B.8 seem to indicate that the

no clamping assumption is a good assumption in this case. It is expected that the more rigid the clamping is on the physical leaf spring the closer it will be to ideal clamping. With a less rigid (or less stiff) clamped section the clamping will be closer to the no clamping assumption.

### B.3. Additional validation tests

Figure B.8 showed good correlation between the theoretical calculated stiffness and the stiffness observed on the experimental force-displacement characteristic of the multi-leaf spring. Comparisons of the theoretical and experimental stiffness of three additional leaf spring configurations will be presented. The theoretical calculations will be done for both the ideal clamping and no clamping assumption. The three additional tests were performed with the leaf spring having three full length blades. Each test used a different physical clamped length:

Test 1: 3 blade, clamped length = 0.076m

Test 2: 3 blade, clamped length = 0.22m

Test 3: 3 blade, clamped length = 0m

Additional to these three tests, a fourth test was performed with the original leaf spring (having three full length blades and 5 non-full length blades) and a clamp length of 0m but the test setup broke and the measured data was not useful. A detailed discussion of each of the tests is given in the following sections. Note that for calculation of stiffness using the SAE spring design manual (1996) a stiffening factor ( $SF$ ) of 1.5 is used when all blades are full length.

#### B.3.1 Test 1: 3 blade, clamped length = 0.076m

Figure B.9 shows the experimental setup of the 3 blade, full length leaf spring. The five non-full length blades were rotated 90 degrees and created a clamped length of 0.076m. Figure B.10 shows the correlation between the theoretical and experimental stiffness for this configuration with the ideal clamping assumption. Figure B.11 shows the results for the no clamping assumption.

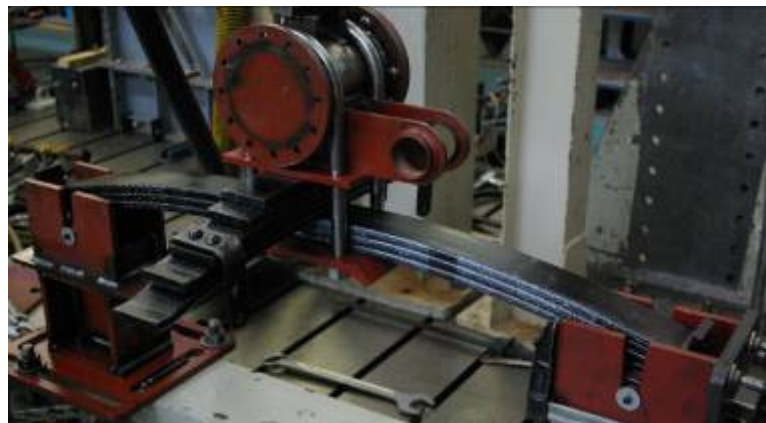


**Figure B.9.** Experimental setup of leaf spring with three full length blades and clamp length = 0.076m

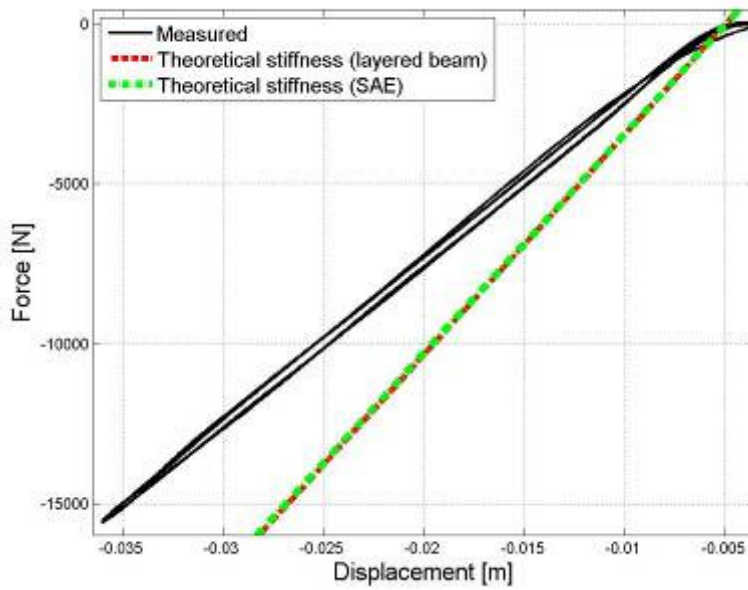


**Figure B.10.** Comparison between measured and theoretical stiffness for test 1 assuming ideal clamping

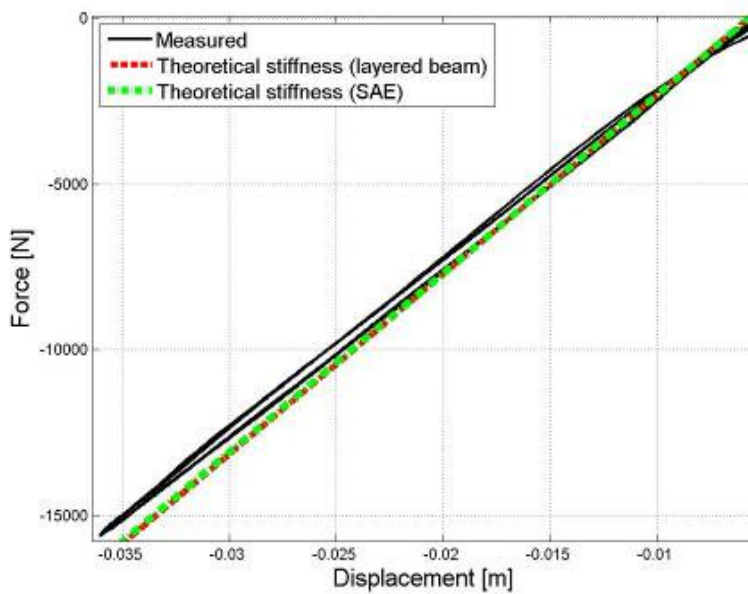


**Figure B.11.** Comparison between measured and theoretical stiffness for test 1 assuming no clamping

### B.3.2 Test 2: 3 blade, clamped length = 0.22m

This test setup is shown in Figure B.12. When the theoretical stiffness, calculated using the ideal clamping assumption, is compared to the measured stiffness it is again observed that the theoretical stiffness is higher (see Figure B.13). Figure B.14(a) shows the correlation between the measured and theoretical stiffness when no clamping is assumed in the clamped section. With the assumption of no clamping being present in the clamped section the theoretical stiffness is lower than the measured stiffness. However, if a clamping is assumed that lies between the ideal and no clamping conditions the resulting theoretical stiffness correlates well with the measured stiffness (see Figure B.14(b)). The clamping between the ideal and no clamping conditions were simulated by setting the theoretical clamped length equal to 0.1m.



It was expected that if the no clamp assumption was used in the theoretical calculation of the stiffness will again show good correlation to the measured stiffness.

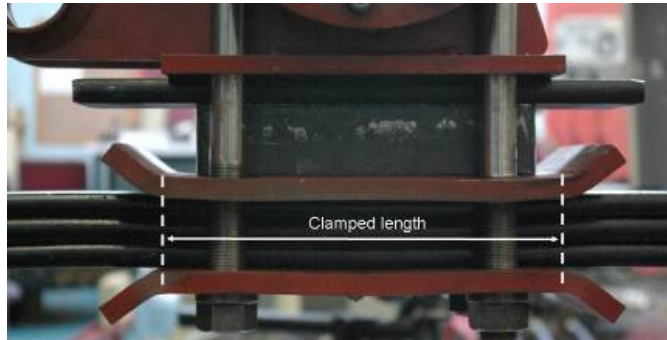


Figure B.12. Experimental setup of leaf spring with three blades and clamp length = 0.22m

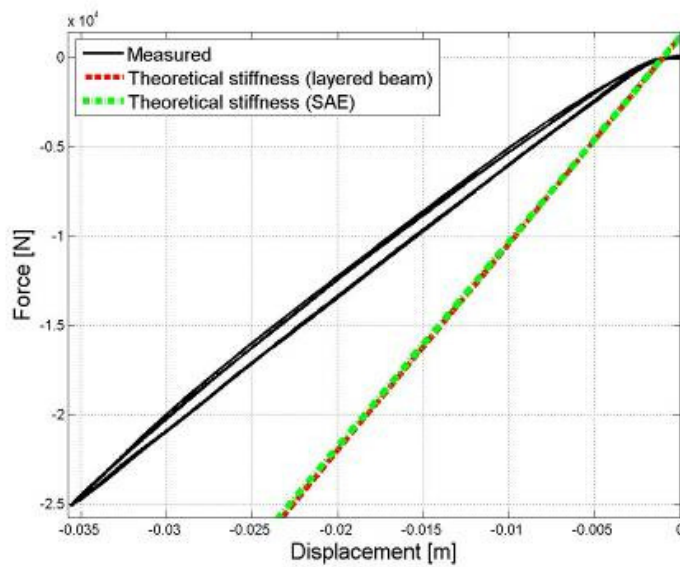


Figure B.13. Comparison between measured and theoretical stiffness for test 2 assuming ideal clamping

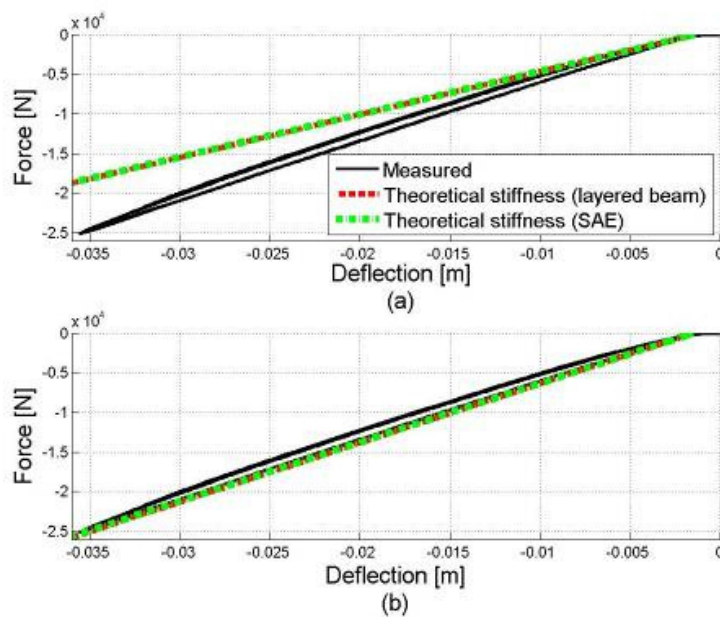
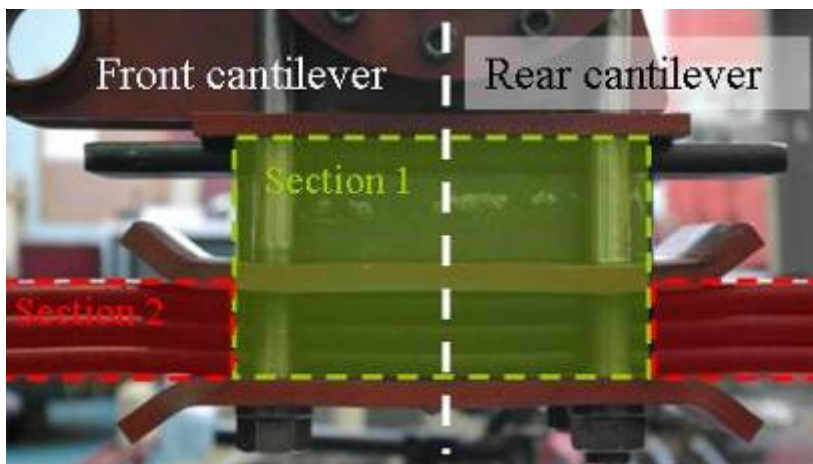
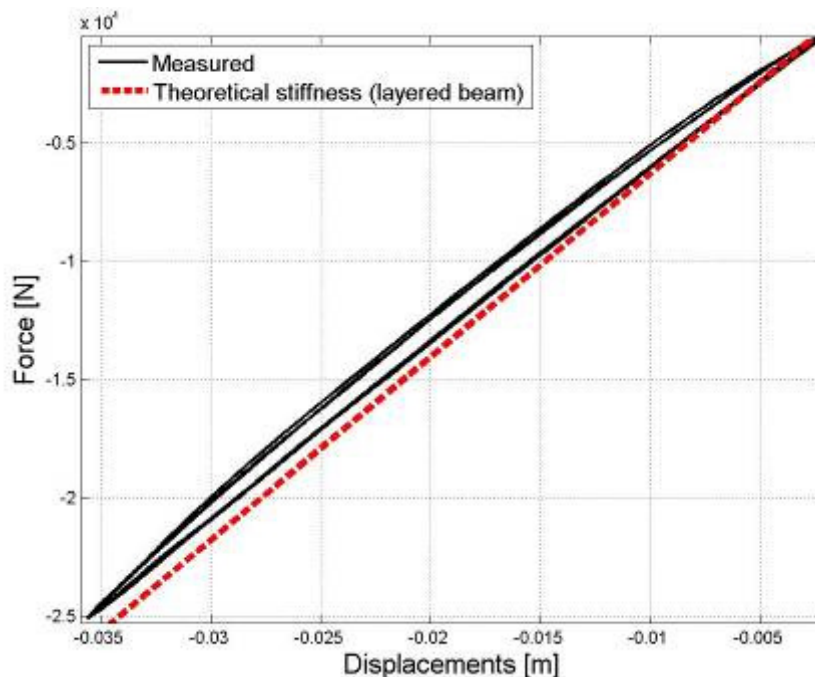


Figure B.14. Comparison between measured and theoretical stiffness for test 2 (a) Assumed no clamping . (b) Assumed clamping is between ideal and no clamping condition

However, when the setup shown in Figure B.12 is modelled in a different way, the theoretical stiffness obtained, with the no clamp assumption, is improved. The setup was modelled as three full-length prismatic blades. Instead, if the setup is modelled as shown in Figure B.15 the correlation obtained between the measured and theoretical stiffness is good when assuming a no clamping condition within the clamped section. The setup is modelled as having two sections. Section 1 has a length of 0.195m with the height being equal to the height of 8 blades. Section 2 is made up of three full length blades (see Figure B.15). In other words, the leaf spring effectively consisted out of three full length blades with five non-full length blades having equal length. The results using this model and the no clamping assumption are shown in Figure B.16 which correlate well with the measured stiffness. This shows that it is just as important to model the spring's cross-sectional area correctly as it is to model the boundary condition correctly.



**Figure B.15.** Leaf spring modelled as having three full length blades and 5 non-full length blades having equal length



**Figure B.16.** Comparison between measured and theoretical stiffness for test 2 assuming no clamping and using the model shown in Figure B.15

### B.3.3. Test 3: 3 blade, clamped length = 0m

Figure B.17 shows the experimental setup of the leaf spring with 3 full-length blades and a clamp length of 0. Figure B.18 shows the comparison between the theoretical and measured stiffness for this setup. The correlation is not as good as obtained for the test in paragraph B.3.1 and B.3.2 with the theoretical stiffness being higher than the measured stiffness. A possible reason for the physical spring being less stiff than the theoretical values may be due to the presence of the hole of the centre bolt. This was investigated by including the hole in the theoretical calculations to see whether this has any effect.



**Figure B.17.** Experimental setup of leaf spring with three full length blades and clamp length = 0m

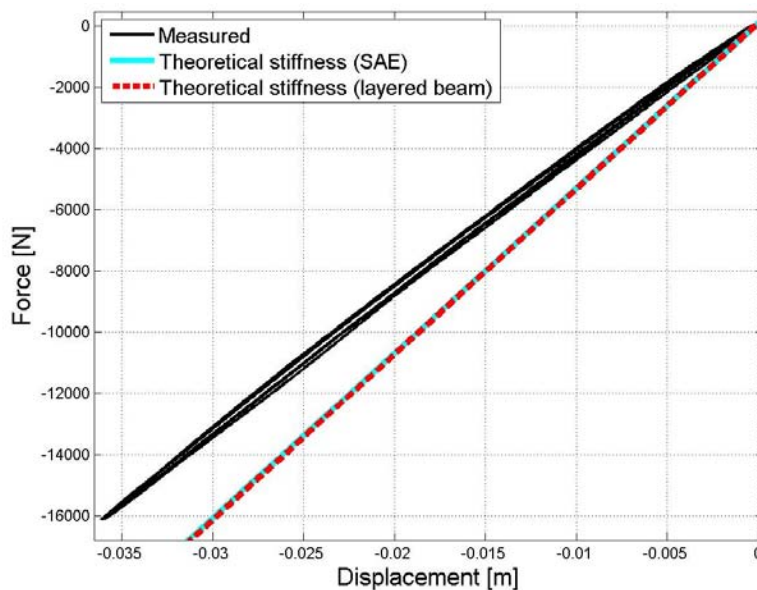


**Figure B.18.** Comparison between measured and theoretical stiffness for test 3

It is postulated that when including the effect of the hole in the theoretical calculation that the correlation shown in Figure B.18 will improve. The hole removes material and should thus decrease the stiffness of the blade as it leads to a smaller area moment of inertia (see Figure B.19). The hole was effectively treated as a square cut-out.



**Figure B.19.** Effect of hole on the area moment of inertia

Figure B.20 shows the comparison between the measured stiffness and the theoretical stiffness, calculated without and with the hole using the method of super position. From the figure it can clearly be observed that the hole does not have a big effect on the theoretical stiffness of the spring. The reason for the deviation between the theoretical and measured stiffness is not clear.

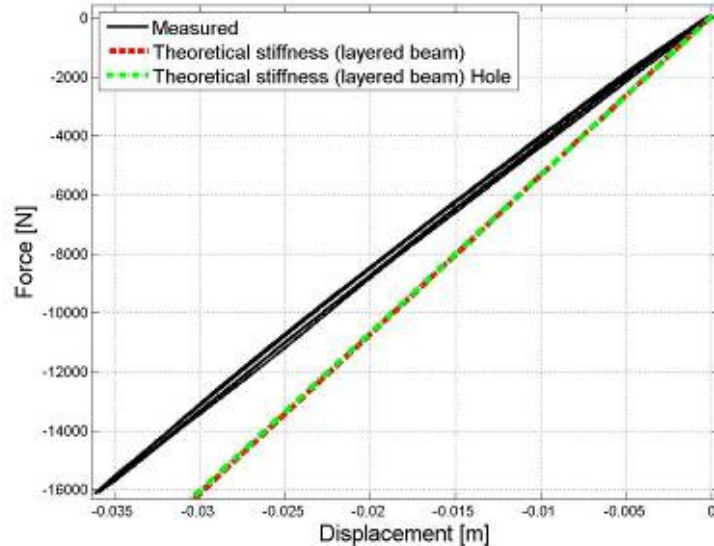


**Figure B.20.** Comparison between measured and theoretical stiffnesses (with and without hole) for test 3

## B.4. Conclusion

The theoretical calculation of the stiffness of the two regimes in the force-displacement characteristic of the multi-leaf spring was investigated. It was shown that the stiffness regimes can be calculated using simple beam theory. The effect of the clamping assumption on the theoretical stiffness was shown. The clamping assumption influences the boundary conditions which is a similar effect that was obtained during the experimental characterisation in Chapter 2. It was shown in Chapter 2 that the stiffness of the spring is sensitive to the U-bolt preload which governs how the leaf spring is constrained and is analogue to the clamping assumption which governs the boundary condition. The sensitivity that was shown by the theoretical stiffness calculation with respect to the clamping assumption and the loaded length shows good agreement to what was observed during the experimental characterisation of the leaf spring.

The results in this appendix confirmed that the postulate of the two stiffness regimes being representative of a layered beam and solid beam behaviour is true. The results also indicate that the method can be used to theoretically calculate the stiffness of a multi-leaf spring. This method should be used on different leaf springs to confirm that it is generally applicable. It is suggested that the theoretical stiffness be used as a good estimator of the stiffness that can be expected for a specific leaf spring. The equation presented to calculate the stiffness of the layered leaf spring assumes that there is no friction present between individual blades. Future work should investigate ways to account for the friction between the blades in order to quantify the hysteresis loop. With the ability to account for the hysteresis and combining it with the theoretical stiffness of the two regimes will imply that the force-displacement characteristic can be calculated theoretically. This will be useful during early stages in the product development stage when physical leaf springs are not yet available or the configuration of the leaf spring is to be determined. This method will also enable the elastoplastic leaf spring to be parameterised theoretically